Ab initio based ligand field approach to determine electronic multiplet properties

R Kuzian, O Janson, Adrien Savoyant, Jeroen van den Brink, R Hayn

Ab initio based ligand field approach to determine electronic multiplet properties

R. O. Kuzian,[1,2] O. Janson,[3] A. Savoyant,[2] Jeroen van den Brink,[3] and R. Hayn[2,3]
[1]*Institute for Problems of Materials Science NASU, Krzhizhanovskogo 3, 03180 Kiev, Ukraine*
[2]*Aix-Marseille Université, IM2NP-CNRS UMR 7334, Campus St. Jérôme, Case 142, 13397 Marseille, France*
[3]*Leibniz Institute for Solid State and Materials Research IFW Dresden, 01171 Dresden, Germany*

(Received 1 June 2021; accepted 27 July 2021; published 30 August 2021)

A method is developed to calculate the ligand field (LF) parameters and the multiplet spectra of local magnetic centers with open d and f shells in solids in a parameter-free way. This method proceeds from density functional theory and employs Wannier projections of nonmagnetic band structures onto local d or f orbitals. Energies of multiplets and optical, as well as x-ray spectra are determined by exact numerical diagonalization of a local Hamiltonian describing Coulomb, LF, and spin-orbit interactions. The method is tested for several $3d$ and $5f$ compounds for which the LF parameters and multiplet spectra are experimentally well known. In this way, we obtain good agreement with the experiments for La_2NiO_4, $CaCuO_2$, Li_2CuO_2, ZnO:Co, and UO_2.

DOI: 10.1103/PhysRevB.104.085154

I. INTRODUCTION

A fundamental problem in electronic structure theory of solids is the proper description of multiplet effects of local magnetic centers built up of d or f electrons, which are intrinsically many-body states, in translational invariant settings. Electronic structure calculations based on density functional theory (DFT) are successful in predicting the atomic positions, the electronic, magnetic, and state densities in an *ab initio* manner with high precision. However, these calculations use a mean-field potential and one-electron states, and thus in principle cannot access the many-electron multiplet levels characterized by strong Coulomb interactions, electron correlations, and spin orbit coupling. However, the structure of local multiplets is well understood since many years in atomic physics, mainly based on group theory applied to open-shell atoms or ions. Such multiplets can persist in solids, either as sharp levels in the gap of insulators or semiconductors or as resonances in metals and small gap semiconductors. The difference to the case of isolated atoms and ions is the appearance of a small number of new parameters which effectively describe the influence of the surrounding crystal. Traditionally, they are often called crystal field (CF) [1] parameters since they are partially caused by the electrostatic Madelung potential in the crystal. However, in most cases, and especially in the examples of $3d$ and $5f$ compounds we are going to treat, the hybridization to the neighboring ligands, also known as ligand fields (LF), makes a much bigger influence and that is the term which we will prefer here. Without explicit hybridization with neighboring orbitals, a given set of LF parameters determines entirely the influence of the environment on the multiplet structure of a localized open d or f shell.

The knowledge of LF parameters and multiplet spectra is especially important for strongly correlated systems being of high actual interest since they may show superconductivity [2], multiferroism [3,4], or spin liquid behavior [5–7], as well as many other interesting properties. Recently, new experimental techniques like resonant inelastic x-ray scattering (RIXS) lead to important improvements to measure multiplet spectra for cuprates, nickelates [8,9] and other materials.

In the literature, one can find several approaches to calculate LF or CF parameters. First of all, there are wave function quantum chemistry methods [10]. However, it is difficult for these methods to treat a periodic crystal and they become numerically expensive for heavy ions and large systems. This motivates attempts to calculate multiplets and LF parameters in an *ab initio* style and based on DFT [11–13]. Since we are dealing here with highly correlated systems it is tempting to start with the local spin density (LSDA) or spin dependent generalized gradient approximation (SGGA) corrected for Hubbard correlation effects, i.e., the LSDA+U or SGGA+U functionals. And indeed the CF parameters of lanthanide and actinide dioxides were successfully calculated by Zhu and Ozoliņš [14] based on the LSDA+U method with occupation matrix control. However, it is necessary in that case to correct the LSDA+U functional for self-interaction and double counting terms and to modify it. Instead, we here use a simpler method by starting with the original non spin-polarized GGA functional [15]. Similar to the approach of Ref. [4], we obtain then the LF parameters by a Wannier fit to the nonmagnetic band structure. In our method, the strongly correlated $3d$ and $5f$ electrons are included into the charge self-consistency which is, however, not possible for $4f$ electrons. Therefore, our approach is not directly applicable to $4f$ systems, unless we do not go over to the slightly more sophisticated method presented in Ref. [12]. Further, in a second step, we use the LF parameters in an exact diagonalization computer program to predict the outcome of a multitude of experiments being sensible to local multiplet effects, i.e., electron paramagnetic

resonance (EPR), optical spectroscopy, inelastic neutron scattering (INS), x-ray absorption and x-ray magnetic circular dichroism (XAS and XMCD) as well as resonant inelastic x-ray scattering (RIXS). That computer program ELISA (electrons localized in single atoms) was successfully used before to analyze the XAS and XMCD spectra of Mn-based metal-organic networks [16] so that we will concentrate here on the other experimental techniques. In the present publication, we test our method for La_2NiO_4, $CaCuO_2$, Li_2CuO_2, Co impurities in ZnO, and UO_2.

In our approach, we calculate the influence of the neighboring ligands on the local one-electron energy levels of the d or f center, i.e., the LF parameters. We then diagonalize exactly the local, atomic like, multiplet Hamiltonian and do not treat the ligand p orbitals explicitly. That is different to the *ab initio* multiplet LF theory of Haverkort *et al.* [17]. Our approach is simpler, and yet fully justified as long as charge-transfer processes in optics or x-ray spectroscopy are not at play. Finally, we obtain various *ab initio* simulations of multiplet spectra without any adjustable parameters others than the line width. Calculating the LF parameters has also the advantage to establish a connection to traditional crystal field methods with parameters obtained by fitting to experimental data.

II. METHOD

The multiplet spectrum of a local d or f center depends on the local Coulomb interaction, the spin-orbit coupling and the LF parameters. The Coulomb and spin-orbit parameters of the free ion can either be obtained by Hartree-Fock calculations [18,19] or by fitting the optical spectra of free ions. These data are easily accessible in the NIST data set [20] and that is the way we follow here. The Coulomb parameter are usually slightly screened in the solid but we will show that this screening has only little influence on the multiplet spectrum, especially in the low-energy part we are mostly interested in.

In a second step, we perform GGA calculations to obtain the non spin-polarized band structure. These density functional theory calculations were performed here using the full-potential local-orbital (FPLO) code [21,22]. We have used the default FPLO basis. The exchange and correlation potential of Ref. [15] was employed, i.e., the generalized gradient approximation (GGA) functional. Wannier functions (WF) were constructed via projection onto the respective d or f orbitals of a magnetic atom; the site symmetry is fully taken into account; as it is implemented in the FPLO code [23]. We first do this "Wannier fit" for the scalar relativistic case and obtain then the LF parameters by a fit to the on-site energies of the Wannier expansion. Next, we perform the same procedure for the full relativistic, but nonmagnetic GGA functional. That does not change the LF parameters, but opens the possibility to calculate also the spin-orbit parameter being reduced in the solid with respect to the free ion value. A remarkable reduction was observed for the cuprates which we investigate and will be discussed in detail later on.

The final step of our method consists in the exact diagonalization of an electronic Hamiltonian within the finite state space of open atomic shell(s) using the ELISA code. That code is able to treat several electronic configurations, an arbitrary number of electrons in each shell, and contains all the Coulomb interactions within one shell and between different shells. The influence of the surrounding ligands is taken into account by a LF Hamiltonian written in terms of Steven's operators with appropriate symmetry. The Hamiltonian contains Coulomb interaction, the ligand field, the spin-orbit coupling, and the magnetic field:

$$\hat{H} = \hat{H}_{\mathrm{Coul}} + \hat{H}_{\mathrm{LF}} + \hat{H}_{\mathrm{SO}} + \hat{H}_{\mathrm{B}}. \tag{1}$$

In the examples treated in the present study we are going to consider $2p$, $3d$, and $5f$ shells. To describe x-ray transitions we have to consider at least two different configurations. The Coulomb interaction

$$\hat{H}_{\mathrm{Coul}} = \frac{1}{2}\sum_{m_i\sigma\sigma'} V_{m_1m_2m_3m_4} c^{\dagger}_{m_1\sigma} c^{\dagger}_{m_2\sigma'} c_{m_3\sigma'} c_{m_4\sigma} \tag{2}$$

is treated as in rotationally invariant atoms and parametrized by Slater parameters. For instance, the Coulomb interaction in the $3d$ shell is given by

$$V_{m_1m_2m_3m_4} = 25\sum_{k=0,2,4}(-1)^{m_1+m_4}F^{(k)} \times \left[C^{k,0}_{2,2,0,0}\right]^2 C^{k,m_3-m_1}_{2,2,m_3,-m_1} C^{k,m_4-m_2}_{2,2,m_4,-m_2} \tag{3}$$

with three Slater parameters $F^{(k)}$ which can also be expressed by three Racah parameters in the form $F^{(0)} = A + \frac{7}{5}C$, $F^{(2)} = 49B + 7C$, and $F^{(4)} = \frac{441}{35}C$. $C^{k,m}_{l_1,l_2,m_1,m-m_1}$ are the usual Clebsch-Gordon parameters in the $3d$ shell when $l_1 = l_2 = 2$. A similar expression holds also for the Coulomb interaction in other shells and in between different shells. The crystal environment influences the spectra by the electrostatic Madelung potential (crystal field) but also by hybridization to the neighboring ligands. Since the second contribution is probably dominant in most cases we prefer the term ligand field Hamiltonian here. It is a noninteracting Hamiltonian, like also the spin-orbit coupling and the Zeemann term, which can be written as

$$\hat{H}_{\mathrm{LF}} + \hat{H}_{\mathrm{SO}} + \hat{H}_{\mathrm{B}} = \sum_{ij}\left(h^{ij}_{\mathrm{LF}} + h^{ij}_{\mathrm{SO}} + h^{ij}_{\mathrm{B}}\right)c^{\dagger}_i c_j \tag{4}$$

and which are quadratic in the Fermi creation $c^{\dagger}_i$ and annihilation c_j operators with the combined indices $i = \{m, \sigma\}$ and $j = \{m', \sigma'\}$. The LF part

$$h^{ij}_{\mathrm{LF}} = H_{mm'}\delta_{\sigma\sigma'} \tag{5}$$

can be expressed in terms of Steven's operators. That part is specific to each of the following examples and will be detailed there. Finally, the spin-orbit coupling and the Zeemann term

$$h^{ij}_{\mathrm{SO}} + h^{ij}_{\mathrm{B}} = \zeta\langle i|\hat{\vec{s}}\,\hat{\vec{l}}\,|j\rangle + \mu_B\vec{B}\langle i|\hat{\vec{l}} + g_s\hat{\vec{s}}\,|j\rangle \tag{6}$$

are expressed as matrix elements of the one-particle spin and orbital momentum operators, and where $g_s = 2.0023$ is the

free electron gyromagnetic ratio. Please remind, that the parameters of the one-particle Hamiltonian are obtained by DFT calculations, but the Coulomb parameters from free ions.

To calculate the optical and x-ray spectra, the dipole transition probabilities are calculated in the ELISA code as it was already published for XAS and XMCD [16]. To determine the RIXS intensity, we use the formula

$$I(\omega) = \sum_f \delta(\omega_{\text{in}} - \omega_{\text{out}} - (E_f - E_i))|A_f|^2, \tag{7}$$

where $\omega = \omega_{\text{in}} - \omega_{\text{out}}$ is the energy transfer, the indices i and f denote initial and final states, respectively, and with the scattering amplitude

$$A_f = A_f(\omega_{\text{in}}) = \sum_m \frac{\langle f|\vec{E}_{\text{in}} \cdot \vec{r}|m\rangle\langle m|\vec{E}_{\text{out}} \cdot \vec{r}|0\rangle}{\omega_{\text{in}} - (E_m - E_i) + i\Gamma} \tag{8}$$

where we sum over all intermediate states m. The optical absorption spectra are calculated by using the approach of Sugano and Tanabe [24] where the d-d transitions between two states a and b become possible by combining a parity changing perturbation V_{odd} with the dipole operator $\vec{P} = q \cdot \vec{r}$ to give the transition probability by

$$W = \left| \frac{2}{\Delta E} \langle a|V_{\text{odd}}\vec{P}|b\rangle \right|^2, \tag{9}$$

where ΔE is the energy difference between the given configuration with incomplete d shell and the first excited configuration with odd parity. We applied this option of ELISA to the case of ZnO:Co and specify the parity breaking perturbation later on.

III. RESULTS

A. Nickelate La_2NiO_4

That compound is a 2D antiferromagnet and an interesting reference material for 2D cuprates since it shares the same crystal structure. However, in difference to the famous La_2CuO_4 [2,25], the local spin is not $S = 1/2$ but $S = 1$, instead. The presence of a $3d^8$ configuration in a tetragonal environment allows for interesting multiplet effects and we will use it here to demonstrate our method. The main focus is to calculate, without adjustable parameter, the RIXS spectra of Ni^{2+} in La_2NiO_4 which were recently measured [9] and to compare our method with quantum chemical wave function methods [26]. To simulate the RIXS spectra, we use two configurations in the ELISA code, namely, the $3d^8 2p^6$ ground-state configuration of initial and final states as well as the excited-state configuration with one core-hole $3d^9 2p^5$ for the intermediate states of the RIXS scattering process. The Hamiltonian contains all the Coulomb interactions within each of the $3d$ and the $2p$ shells as well as between both shells. The influence of the six surrounding oxygen ligands (tetragonal ligand field) is taken into account by a ligand field Hamiltonian written in terms of Steven's operators.

1. Free ion

The above Hamiltonian (1) without the ligand-field H_{LF} and Zeeman H_{B} parts, describes already very well the energy level scheme of a free Ni^{2+} ion (NIST data base [20]). That fixes the intra-d Coulomb parameters to $F^{(2)} = 9.8$ eV and $F^{(4)} = 6.1$ eV, as well as a small spin-orbit coupling in the $3d$ shell of $\zeta = 80$ meV. The Slater parameter $F^{(0)}$ is not relevant since initial and final states have the same number of d electrons. In Table I, we show the very good agreement between experimental and calculated levels.

TABLE I. Comparison of the experimental free ion levels of Ni^{2+} from the NIST data set [20] with the ELISA calculation using the parameters given in the text.

Notation	ELISA (eV)	NIST (eV)
$^3F_4$	0.00	0.00
$^3F_3$	0.162	0.168
$^3F_2$	0.272	0.281
$^1D_2$	1.715	1.739
$^3P_2$	2.085	2.066
$^3P_1$	2.125	2.105
$^3P_0$	2.156	2.136
$^1G_4$	2.663	2.865
$^1S_0$	6.399	6.513

2. Wannier fit

Stoichiometric La_2NiO_4 features an involved phase diagram with an orthorhombic and two tetragonal phases [27]. Since the RIXS measurements were carried out at 20 K [9], at which the tetragonal $P4_2/ncm$ structure is dominant [27], we choose this structure for further analysis. Note that despite the tetragonal symmetry, the local z axes of neighboring elongated NiO_6 octahedra are neither mutually parallel, nor coincide with the crystallographic c direction. Moreover, the four short Ni–O bonds split into two pairs of equivalent bonds with the lengths of 1.944 and 1.954 Å, respectively. In the following, we refer to this structure as the experimental structure, to distinguish it from the simplified (fictitious) $I4/mmm$ structure. The lattice constants for the latter are chosen so that the constituent NiO_6 octahedra have a tetragonal point symmetry and the Ni–O bond lengths are as close as possible to those of the experimental structure. Atomic coordinates of both structures are provided in Table II.

We start with scalar-relativistic calculations on $18 \times 18 \times 8$ ($18 \times 18 \times 18$) mesh of k-points for the experimental (simplified) structure. Typical for correlated insulators, the nonmagnetic GGA yields a metallic solution, signalled by the bands crossing the Fermi level (Fig. 1). Site- and orbital-resolved densities of states reveal the dominance of Ni $3d$ states, with a significant admixture of O $2p$ states (Fig. 1, right panels). To construct a minimal model, we perform Wannier projections onto all Ni $3d$ states; the local axes that determine the Wannier orbital basis coincide with the axes of the respective NiO_6 octahedron. We choose the energy window between -2.4 and 2.2 eV (2 eV for the simplified structure), the width of the Gaussian tails is 0.3 eV. In this way, we obtain a good agreement between the Fourier-transformed Wannier Hamiltonian and the GGA band structure (Fig. 1, left panels).

Since we are interested in local processes, we restrict our analysis to local hopping terms t_{ii} comprising the 5×5 onsite

TABLE II. Atomic coordinates of the experimental (sp. gr. $P4_2/ncm$ (138); $a = 5.4995$ Å, $c = 12.5052$ Å) and simplified (sp. gr. $I4/mmm$ (139); $a = 3.8983$ Å, $c = 12.58047$ Å) La_2NiO_4 structures.

experimental La_2NiO_4 structure (from Ref. [27])				
site	Wyckoff position	x/a	y/b	z/c
Ni	4*d*	0	0	0
La	8*i*	−0.0072	−0.0072	0.3639
O	4*e*	1/4	1/4	−0.0155
O	4*a*	1/4	3/4	0
O	8*i*	0.0314	0.0314	0.1771

simplified (fictitious) La_2NiO_4 structure				
site	Wyckoff position	x/a	y/b	z/c
Ni	2*a*	0	0	0
La	4*e*	0	0	0.6361
O	4*c*	0	1/2	0
O	4*e*	0	0	0.8229

Hamiltonian matrix H_{ii}. All Ni sites in either structure are equivalent, hence it is sufficient to consider a single site i. The tetragonal crystal-field parameters D_t and D_s as well as the cubic crystal-field splitting $10D_q$ are obtained by solving the linear problem

$$\begin{pmatrix} 1 & -4 & -1 & 2 \\ 1 & -4 & 4 & -1 \\ 1 & 6 & -6 & -2 \\ 1 & 6 & -1 & 2 \end{pmatrix} \begin{pmatrix} \varepsilon_0 \\ D_q \\ D_t \\ D_s \end{pmatrix} = \begin{pmatrix} \langle d_{xy}|H_{ii}|d_{xy}\rangle \\ \langle d_{yz/xz}|H_{ii}|d_{yz/xz}\rangle \\ \langle d_{3z^2-r^2}|H_{ii}|d_{3z^2-r^2}\rangle \\ \langle d_{x^2-y^2}|H_{ii}|d_{x^2-y^2}\rangle \end{pmatrix}, \tag{10}$$

where the coefficients of the matrix are adopted from Ref. [29]. The vector in the right-hand side of the equation comprises diagonal elements of H_{ii} listed in Table III together with the resulting crystal-field parameters for both structures.

Another key parameter that we can extract from DFT calculations is the $3d$-shell spin-orbit coupling constant ζ. To this end, we perform full-relativistic nonmagnetic GGA calculations, followed by a wannierization (see Appendix A for details). We focus again on the onsite Hamiltonian matrix H_{ii}, which is now a 10×10 matrix due to the presence of two spin channels. Let us start with the simplified structure. Here, the H_{ii} in Table XIII has precisely the same form as the sum of the diagonal crystal-field and the atomic spin-orbit (Table XIV) contributions. Since the latter has only one free parameter, the spin-orbit coupling constant ζ, we can estimate it by comparing the respective off-diagonal matrix elements of H_{ii} with that of Table XIV. Since the latter imply the local cubic symmetry which is higher than the tetragonal symmetry of our simplified structure, different matrix elements give slightly different values of ζ. By averaging over all matrix elements, we obtain $\zeta = 73 \pm 3$ meV.

Now we turn to the more complicated case of the experimental structure. Here, the matrix form of H_{ii} in Table XII substantially differs from that of the simplified structure. The reason is twofold. First, the local symmetry of Ni sites is orthorhombic. As a result, some off-diagonal matrix elements in the crystal-field Hamiltonian become nonzero. Second, the x axis of the coordinate system utilized by FPLO does not coincide with the local x axis of NiO_6 octahedra; a $\frac{3}{4}\pi$ rotation would put it in place. While the current version of FPLO does not allow the user to choose the direction of the x axis, we can rotate the basis of the matrix describing the atomic SOC such that it has the same form as our H_{ii}. The technical details of this transformation are described in Appendix A 3. In this way, we obtain $\zeta = 74 \pm 2$ meV, which is in excellent agreement with the value obtained for the simplified structure.

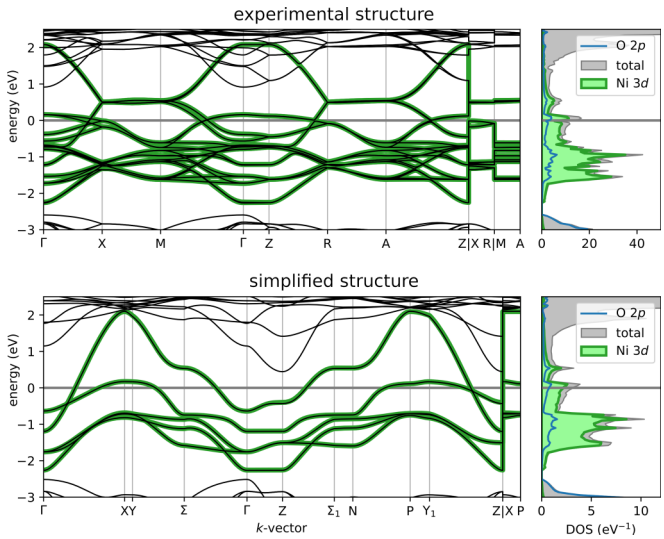

FIG. 1. GGA band structures (thin black lines) and Fourier-transformed Wannier projections onto Ni $3d$ states (thick green lines) for the experimental (top) and simplified (bottom) structure of La_2NiO_4. Note that the experimental structure features two Ni sites per cell giving rise to ten $3d$ bands, while the simplified structure has only one Ni site per primitive cell, and hence only five bands. The right panels show the densities of states (DOS): total (gray-shaded), Ni $3d$ (green-shaded), and O $2p$ (blue). For the notation of k vectors, see Ref. [28]. The Fermi level is at zero energy.

3. *Multiplet spectra*

In the given case of tetragonal symmetry, the ligand-field part of the Hamiltonian writes:

$$\hat{H}_{\mathrm{LF,t}} = B_{20}\hat{O}_2^0 + B_{40}\hat{O}_4^0 + B_{44}\hat{O}_4^4, \tag{11}$$

where the explicit expressions of the Steven's operators are repeated in the Appendix B. Sometimes, the three crystal field parameters are expressed differently by

$$D_q = \frac{12}{5}B_{44},\ D_s = 3B_{20},\ D_t = \frac{12}{5}B_{44} - 12B_{40}. \tag{12}$$

To calculate the multiplet spectrum (see Table IV), we use the parameters $10D_q = 1.5835$ eV, $D_s = 0.0584$ eV, and $D_t = 0.0461$ eV; corresponding to $B_{44} = 65.98$ meV, $B_{40} = 9.35$ meV, and $B_{20} = 19.47$ meV; as obtained from a Wannier

TABLE III. Diagonal matrix elements of H_{ii} obtained using Wannier projections onto Ni $3d$ states for scalar-relativistic (no SOC) and full-relativistic (with SOC) GGA calculations of the experimental as well as the simplified structure of La_2NiO_4. The cubic ($10D_q$) and tetragonal (D_t, D_s) crystal-field parameters are calculated via Eq. (10). All values are in meV.

	experimental structure		simplified structure	
	no SOC	with SOC	no SOC	with SOC
$\langle d_{xy}\|H_{ii}\|d_{xy}\rangle$	−1246.7	−1250.1	−1250.6	−1254.9
$\langle d_{yz}\|H_{ii}\|d_{yz}\rangle$	−1190.4	−1193.7	−1197.1	−1200.4
$\langle d_{3z^2-r^2}\|H_{ii}\|d_{3z^2-r^2}\rangle$	−1189.7	−1195.8	−1197.1	−1200.4
$\langle d_{xz}\|H_{ii}\|d_{xz}\rangle$	−126.8	−130.6	−125.1	−131.2
$\langle d_{x^2-y^2}\|H_{ii}\|d_{x^2-y^2}\rangle$	336.5	333.4	329.8	329.9
$10D_q$	1583.2	1583.5	1580.4	1584.9
D_t	46.2	46.1	45.1	45.8
D_s	58.1	58.4	57.3	58.1

fit to the bandstructure of the nonmagnetic DFT solution of La_2NiO_4 in the realistic tetragonal structure. In Table IV, we compare the Wannier parameter spectrum with the experimental one as obtained by RIXS, as well as with a spectrum obtained by a quantum chemical wave function method using the complete-active-space self-consistent-field (CASSCF) and multireference configuration-interaction (MRCI) techniques, finding a good agreement.

4. RIXS

To determine the RIXS intensity we use the Eqs. (7) and (8). For the Ni L_3-edge RIXS measurements, the intermediate states are those of the $2p^5 3d^9$ excited configuration, made of two open shells. They are separated by 855 eV from the ground configuration containing the initial and final states. The ELISA program can treat all interactions within and in between the two configurations. In addition to the three Coulomb parameters of the $3d$ shell, we use the Coulomb interaction of the $2p$ shell $F^{(2)}_{2p} = 6$ eV, intershell Coulomb parameters $F^{(2)}_{pd} = 5.81$ eV, $G^{(1)}_{pd} = 4.32$ eV, and $G^{(3)}_{pd} = 2.46$ eV. These parameters are obtained from a Hartree-Fock solution [18,19] of the free ion, but they are not critical for the RIXS spectra.

The inclusion of the core-hole configuration does not influence the energy level scheme of the $3d^8$ configuration. It is just needed to calculate the matrix elements of the scattering amplitude. The energy of the incoming x rays ω_{in} is chosen such that we integrate over all states of the $J = 3/2$ manifold, i.e., we restrict ourselves to the L_3 edge. The SO coupling splits the ground-state triplet $^3B_{1g}$ (see Table IV) into a lower singlet (B_{2g}) and an upper doublet (E_g) which are separated by 1.1 meV in our approach, and by 2.1 meV in quantum chemistry [26]. The directions of the electric field for incoming and outgoing x rays are dictated by the experimental geometry (see Fig. 8.6 c in Ref. [26]). The incoming x rays are linearly polarized, either perpendicular (σ polarization) to the scattering plane or within the scattering plane (π polarization). The c axis is directed perpendicular to the surface and the incoming x ray has an angle of Θ with the surface. The angle between incoming and outgoing x rays is fixed to $\alpha = 50^\circ$. Accordingly, the direction of the electric field for the incoming beam with π and σ polarization is given by

$$E^{\pi}_{\text{in}} = \sin\Theta\vec{e}_x + \cos\Theta\vec{e}_z, \qquad E^{\sigma}_{\text{in}} = \vec{e}_y. \tag{13}$$

For both cases, we sum the intensities for both possible polarizations of the outgoing beam, i.e.,

$$E^{(1)}_{\text{out}} = \sin(\Theta+\alpha)\vec{e}_x + \cos(\Theta+\alpha)\vec{e}_z, \qquad E^{(2)}_{\text{out}} = \vec{e}_y. \tag{14}$$

In Fig. 2, we compare the calculated spectra with experiment [9]. We choose an income angle of $\Theta = 20^\circ$ since there exist detailed data showing a pronounced dichroism for that income angle. We also calculated the RIXS spectra for other income angles (not shown) and find generally a good agreement with experiment as concerns the main peak positions, its relative weight, and angle dependence. The experimental low-energy peak at about −0.1 eV energy loss is shifted from the zero of energy due to a local exchange field of the neighboring spins in the antiferromagnetic structure which is possible for an income angle of $\Theta = 20^\circ$ and is situated at zero energy in the theoretical curve.

TABLE IV. Comparison of multiplet energies of La_2NiO_4 as obtained from the ELISA program with LF parameters from a Wannier fit with quantum chemical calculations (QC) [26] and experimental RIXS data [9]. (Spin-orbit coupling neglected for simplicity).

Notation	Quantum chemistry [26] (eV)	This work (eV)	Experiment [9] (eV)
$^3B_{1g}$	0.00	0.00	0.00
^3E_g	0.74	1.15	1.06
$^3B_{2g}$	1.30	1.58	1.61
$^3A_{2g}$	1.46	2.04	1.61
$^1A_{1g}$	1.66	1.81	1.61
^3E_g	1.73	2.24	2.29
$^1B_{1g}$	1.92	1.94	2.29
^1E_g	2.59	3.03	2.93

B. High-T_c parent compound $CaCuO_2$

Soon after the discovery of high-T_c superconductivity in doped La_2CuO_4 [2], P. W. Anderson [30] realized that strong correlations in the copper $3d$ shell and the quasi-two-dimensional layered structure of this and related copper oxide compounds are substantial for the understanding of their physics [25]. The common structural unit for the rich family

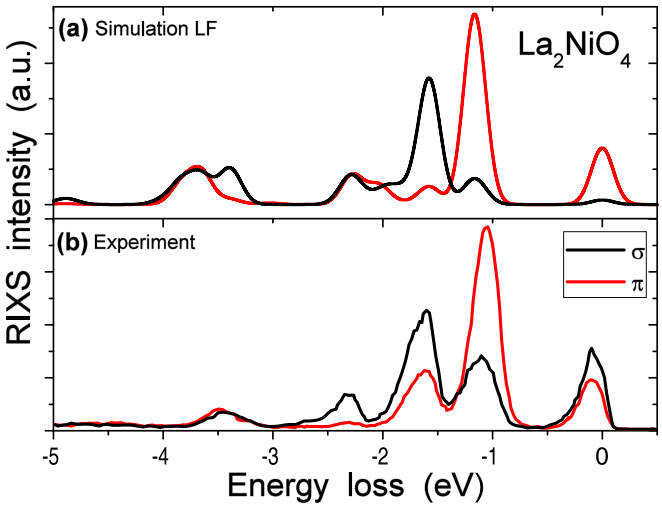

FIG. 2. Comparison of experimental [9] and theoretical RIXS spectra for π and σ polarization and an income angle of $\Theta = 20^\circ$ (The Gaussian broadening of the theoretical curve was set to 0.24 eV; see text for more details).

of cuprate high-T_c superconductors is the CuO_2 plane that is built from corner-shared CuO_4 plaquettes. In each plaquette, the Cu^{2+} ion is surrounded by a square of four oxygen ligands. The LF strongly splits the Cu $3d$ levels so that only the $d_{x^2-y^2}$ orbital hybridized with oxygen p_σ orbitals contributes to the states in the vicinity of Fermi energy and defines the low energy physics of the high-T_c cuprates. The so-called parent (undoped) compounds contain exactly one hole per CuO_4 plaquette. The strong correlations suppress charge fluctuations. The low-energy physics is defined by spin degrees of freedom. The parent compounds are charge-transfer insulators described by the antiferromagnetic Heisenberg Hamiltonan. The localized holes reside mainly on the copper $d_{x^2-y^2}$ orbitals. A doping introduces extra holes or electrons into the CuO_2 planes. With the increase of carrier concentration, the system becomes metallic and superconducting.

The $CaCuO_2$ is a so-called infinite-layer compound, with equal distances between the CuO_2 planes, which are separated only by Ca cations. Under hole doping, the T_c of superconductivity reaches 110 K [31]. Recently, the discovery of superconductivity in hole doped $NdNiO_2$, which is almost isoelectronic to $CaCuO_2$, renewed the interest to the electronic structure of this compound [32,33].

This undoped layered cuprate has tetragonal space group $P4/mmm$ (No. 123) with lattice parameters $a = b = 3.86$ Å, $c = 3.20$ Å. The band structure and projected densities of states of the nonmagnetic GGA solution are depicted in Fig. 3. The figure shows that the antibonding mixture of oxygen p and copper d states (corresponding to five d-like bands in the band structure) lies within the energy window $-3 < \varepsilon - \varepsilon_F < 2.5$ eV (see Appendix C for the choice of the energy window). Within this window, we have constructed Wannier functions having cubic harmonic symmetry (d_{xy}, d_{xz}, d_{zy}, $d_{x^2-y^2}$, and d_{z^2}). The $d_{x^2-y^2}$ orbital has the highest energy. In the ground state, a hole occupies this orbital and the d-d excitations correspond to electron transitions from low lying d levels to the empty $d_{x^2-y^2}$ orbital. Thus, the d-d excitation energies can be

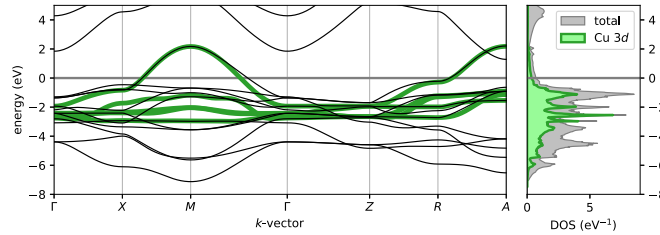

FIG. 3. Band structure (thin black lines) and Wannier projection (thick green lines), as well as densities of states for the high-T_c parent compound $CaCuO_2$. The Fermi level ε_F is set to zero.

calculated by the onsite energy differences $\Delta_i = E_{x^2-y^2} - E_i$ ($E_{x^2-y^2} = \varepsilon_F - 0.094$ eV) for the Wannier functions. These energy differences are given in the second column of Table V and are in good agreement both with sophisticated quantum chemical calculations [10] and experimental values from RIXS measurements [8]. Following Ref. [10], the RIXS energies are corrected by the magnetic energy value $\Delta E_{\text{magn}} = 0.26$ eV.

Then we find the parameters of the Stevens Hamiltonian (11) for $CaCuO_2$ as

$$B_{44} = \frac{1}{24}(E_{x^2-y^2} - E_{xy}) \approx 69.7 \text{ meV}, \tag{15}$$

$$B_{40} = \frac{B_{44}}{5} + \frac{\Delta_t}{105} - \frac{\Delta_g}{140} \approx 1.4 \text{ meV}, \tag{16}$$

$$B_{20} = \frac{1}{21}(\Delta_t + \Delta_g) \approx 123.9 \text{ meV}. \tag{17}$$

where we have introduced the notations $\Delta_t \equiv E_{xy} - (E_{yz} + E_{xz})/2$, $\Delta_g \equiv E_{x^2-y^2} - E_{z^2}$.

Using the so determined LF parameters we can calculate the multiplet spectrum and the RIXS curves. For a d^9 configuration, the energy differences in the multiplet spectrum coincide with the energy differences of the single electron spectrum (see Table V) and they are not at all influenced by the Coulomb parameters. Correspondingly, the peak positions of the RIXS spectra (see Fig. 4) can be interpreted with the help of Table V. In the calculated RIXS spectrum without exchange field [Fig. 4(a)], we can easily distinguish the excitations for d_{xy}, d_{xz}/d_{yz}, and d_{z^2} orbitals at -1.7, -2.0, and -2.2 eV energy loss as single peaks or well developed shoulder. However, the experimental spectrum shows also a magnetic peak due to magnon excitations at -0.4 eV, which we can simulate in our calculation by an exchange field of 0.42 eV acting only on the spin moment and being directed towards the crystallographic

TABLE V. Results for the calculated Cu d-level splitting (in eV) of $CaCuO_2$ compared with quantum chemical calculations [10] and RIXS [8]. Magnetic energy $\Delta E_{\text{magn}} = 0.26$ eV is substracted from each of the RIXS values [10].

	This work	QC	RIXS
$\Delta_{x^2-y^2}$	0	0	0
Δ_{xy}	1.67	1.36	1.38
$\Delta_{zx,zy}$	2.04	2.02	1.69
Δ_{z^2}	2.24	2.38	2.39

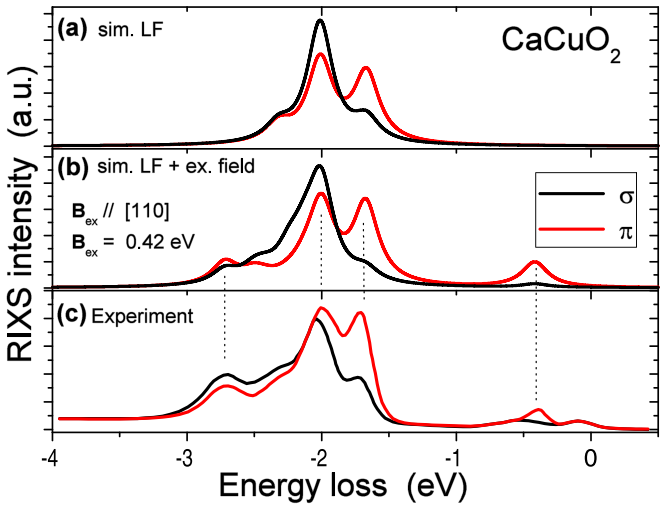

FIG. 4. Comparison of experimental (cf. Fig. 2. of Ref. [8]) and two theoretical (without and with exchange field) RIXS spectra for π and σ polarization and an income angle of $\Theta = 20^\circ$ (The Lorentzian broadening of the theoretical curves was set to 0.23 eV; see text for more details).

[110] direction as in the experimental magnetic structure. It should be noted that an exchange field perpendicular to the Cu-O plane does not lead to a magnetic peak in accordance with the results of theoretical predictions [34]. Interestingly, the inclusion of an exchange field improves also the agreement between experiment and theory at large energy loss and leads to the appearance of peaks between about -2.6 and -2.7 eV energy loss.

C. Quasi-one-dimensional cuprate Li_2CuO_2

The compound Li_2CuO_2 belongs to the family of edge-shared cuprates (ESC). The states near Fermi energy are provided by CuO_4 plaquets that share their edges and form CuO_2 chains. The ESC compounds represent a particular class of quantum magnets in which the local geometry gives rise to competing nearest ferromagnetic or antiferromagnetic exchange coupling J_1 and frustrating antiferromagnetic next-nearest-neighbor J_2 coupling. The one-dimensional spin-1/2 J_1-J_2 Heisenberg model is one prime example of frustrated magnetism, where quantum fluctuations can alter both ground state and spin correlations [35,36]. Due to its simple structure with flat CuO_2 chains, the compound Li_2CuO_2 was considered as a model system for studies of the highly nontrivial magnetism in the edge-shared cuprates [37–48]. Almost two decades passed from the determination of the crystal and magnetic structures of Li_2CuO_2 [37] to a reliable determination of main magnetic interactions within and between the CuO_2 chains [42,49]. This allowed understanding the thermodynamics of the compound [43,45,48] and to demonstrate how the charge-transfer excitation spectra having the scale of several eV are governed by correlations in the spin system with an energy scale $\sim$0.01 eV. This results in strong temperature dependence of the spectra [41,44,46,47].

The space group of the crystal structure is *Immm* (No. 71), lattice parameters are $a = 3.65445$, $b = 2.86022$, and

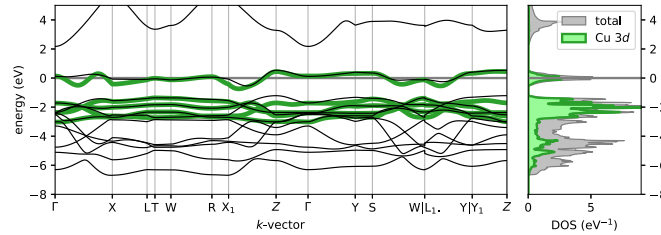

FIG. 5. Band structure (thin black lines) and Wannier projection (thick green lines), as well as densities of states for the quasi-one-dimensional cuprate compound Li_2CuO_2.

$c = 9.3774$ Å. The CuO_2 chains run along b direction in the crystal bc plane. The copper site has $D_{2h}(mmm)$ point group symmetry. It is convenient to take the local coordinate system with the center on the Cu site and the x axis directed along the crystallographic b direction, axis $y \parallel c$, and $z \parallel a$. This coordinate system is rotated by $\pi/4$ around the z axis compared to the one used for $CaCuO_2$. Figure 5 shows that in Li_2CuO_2 the antibonding mixture of oxygen p and copper d states lies within an energy window $-3 < \varepsilon - \varepsilon_F < 0.55$ eV.

In the ground state of Li_2CuO_2, a hole occupies the d_{xy} orbital that lies in the bc plane ($E_{xy} = \varepsilon_F - 0.17$ eV; that orbital would correspond to the $d_{x^2-y^2}$ orbital if we would have chosen the same coordinate system as in $CaCuO_2$). Because of orthorhombic symmetry, the d_{zy} and d_{zx} orbitals are not degenerated and, moreover, a nondiagonal matrix element $V = \langle d_{x^2-y^2}|\hat{H}_{LF}|d_{z^2}\rangle$ is not prohibited by symmetry. However, $V \approx 0$ for the chosen energy window [see Fig. 8(b) in Appendix C]. The LF Hamiltonian for the Cu site in Li_2CuO_2 acquires additional terms compared with $\hat{H}_{\mathrm{LF,t}}$ (11)

$$\hat{H}_{\mathrm{LF,o}} = \hat{H}_{\mathrm{LF,t}} + B_{22}\hat{O}_2^2 + B_{42}\hat{O}_4^2. \tag{18}$$

The parameters of $\hat{H}_{\mathrm{LF,t}}$ found from Eqs. (15)–(17) are $B_{40} \approx -0.55$, $B_{44} \approx -79.1$, and $B_{20} \approx 108.1$ meV. The other parameters are

$$B_{42} = -\frac{1}{42}(E_{zx} - E_{zy}) \approx 3.5 \text{ meV}, \tag{19}$$

$$B_{22} = -3B_{42} \approx -10.5 \text{ meV}. \tag{20}$$

Table VI shows that the energy of d-d excitations obtained from the Wannier function Hamiltonian are in good agreement with the values measured in RIXS experiments and calculated by the elaborated quantum chemical approach [50].

TABLE VI. Results for the calculated Cu d-level splitting (in eV) of Li_2CuO_2 compared with quantum chemical calculations and RIXS [50].

	This work	QC	RIXS
Δ_{xy}	0	0	0
Δ_{zx}	1.82	2.02	2.1
Δ_{zy}	1.96	2.09	2.1
$\Delta_{x^2-y^2}$	1.90	1.55	1.7
Δ_{z^2}	2.28	2.85	2.6

A magnetic induction B_α, $\alpha = x, y, z$ applied along a symmetry axis α splits the ground state doublet according to the effective spin-Hamiltonian

$$\hat{H}_s = g_\alpha \mu_B \hat{s}^\alpha B_\alpha. \tag{21}$$

The g factors are precisely determined in electron paramagnetic resonance experiments. The reported values for Li_2CuO_2 are $g_a \approx 2.264$, $g_b \approx 2.047$, and $g_c \approx 2.033$ [40]. The deviation of g factors from the free electron value g_s characterizes the partial unquenching of the orbital moment due to the spin-orbit interaction.

To calculate the g factors, we need, besides the LF parameters, also the spin-orbit coupling ζ. For that purpose, we performed a Wannier fit for the full-relativistic but nonmagnetic GGA calculation of Li_2CuO_2 (see Appendix A 2). In contrast to La_2NiO_4, we observe a strong covalency reduction k and large deviations from spherical symmetry. The covalency reduction of the free ion spin-orbit (SO) coupling $\lambda_0 = -103$ meV of Cu^{2+} [20] is defined as $\zeta = -k\lambda_0$. (Here, ζ has a positive sign since it is defined for single electrons, whereas λ is defined for the total spin and is negative). Despite the fact that the covalency reduction is usually applied when the rotational symmetry is preserved, we feel justified in the present case of Li_2CuO_2 to take into account only the SO matrix elements with the d_{xy} ground state where the hole resides predominantly. An average over the three relevant matrix elements gives $k = 0.57$ which can be used in the ELISA program to calculate the g factors. With such a procedure we obtain high precision of the low-lying part of the multiplet spetrum but accept deviations at higher energies.

In the given special case of a d^9 configuration, we have a more precise way of determining the g factors by diagonalization of the on-site Hamiltonian matrix in the basis of Wannier functions obtained in the full-relativistic calculation. The calculation (see Appendix A 2 for the details) gives $g_z \approx 2.255$, $g_x \approx 2.062$, and $g_y \approx 2.053$, that is in good agreement with the experimental values. The calculation thus confirms the strong reduction of spin-orbit coupling in Li_2CuO_2.

D. Diluted magnetic semiconductor Co doped ZnO

Co- or Mn-doped ZnO and similar systems were thoroughly studied as diluted magnetic semiconductors in which room-temperature ferromagnetism was predicted due to p-doping [51]. A ferromagnetic-like behavior at room temperature was indeed observed in some samples of ZnO:Co and other doped oxides [52–55]. The origin of this behavior is still under debate [52,56].

The nonmagnetic Zn^{2+} ion of the host lattice is substituted by the Co^{2+} impurity ion having three holes in the $3d$ shell and an effective spin $S = 3/2$. One of the fingerprints of the intrinsic magnetism in ZnO:Co is a strong easy-plane magnetic anisotropy [57]. The anisotropy is due to the single-ion anisotropy of Co^{2+}, which is the consequence of the d-level splitting by the trigonal ligand field generated by a tetrahedral oxygen surrounding [58].

ZnO has wurtzite structure (space group $P6/mmm$ No. 186) with lattice parameters $a = b = 3.2427$ and $c = 5.1948$. A unit cell contains two formula units. The Co impurity is modeled here by the supercell method: we perform DFT calculations for periodic system with unit cells $CoZn_7O_8$ (containing $4 = 2 \times 2 \times 1$ primitive wurtzite unit cells) and $CoZn_{15}O_{16}$ ($8 = 2 \times 2 \times 2$); one Zn atom in the supercell being substituted by Co. The positions of Co and of the surrounding oxygens were relaxed. The $3d$ states of Co form a narrow band within the energy window $-0.75 < E = \varepsilon_F < 0.2$ (see Fig. 6).

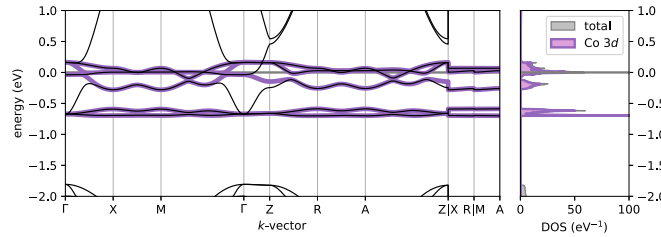

FIG. 6. Band structure (thin black lines) and Wannier projection (thick purple lines), as well as densities of states for a $CoZn_{15}O_{16}$ ($2 \times 2 \times 2$) supercell with relaxed positions of Co and its oxygen neighbors.

For the trigonal field the Hamiltonian in terms of Stevens operators may be written as

$$\hat{H}_{\rm LF} = \hat{H}_{\rm cub} + \hat{H}_{\rm trig}, \tag{22}$$

$$\hat{H}_{\rm cub} = -\frac{2}{3}B_4^0\left(\hat{O}_4^0 - 20\sqrt{2}\hat{O}_4^3\right),$$

$$\hat{H}_{\rm trig} = B_2'\hat{O}_2^0 + B_4'\hat{O}_4^0. \tag{23}$$

The basis of real functions

$$\begin{aligned}
|x\rangle &= \sqrt{\frac{2}{3}}|x^2 - y^2\rangle - \sqrt{\frac{1}{3}}|zx\rangle,\\
|y\rangle &= -\sqrt{\frac{2}{3}}|xy\rangle - \sqrt{\frac{1}{3}}|zy\rangle,\\
|z\rangle &= |z^2\rangle,\\
|v\rangle &= \sqrt{\frac{1}{3}}|x^2 - y^2\rangle + \sqrt{\frac{2}{3}}|zx\rangle,\\
|w\rangle &= -\sqrt{\frac{1}{3}}|xy\rangle + \sqrt{\frac{2}{3}}|zy\rangle
\end{aligned} \tag{24}$$

diagonalizes the cubic part of $\hat{H}_{\rm LF}$ (C_3 axis along z) with an energy splitting Δ. The three basis functions $|x\rangle$, $|y\rangle$, and $|z\rangle$ build up the t_{2g} representation of the tetrahedral cubic group and $|v\rangle$, $|w\rangle$ span up the e_g subspace. The corresponding diagonal on-site matrix-elements are $E_z - E_d = (2/5)\Delta - (2/3)v$, $E_x - E_d = E_y - E_d = (2/5)\Delta + v/3$, and $E_v - E_d = E_w - E_d = -(3/5)\Delta$, all counted from $E_d = (2E_x + E_z + 2E_v)/5$, which is the d-level energy in the absence of ligand field. The trigonal part $\hat{H}_{\rm trig}$ splits the t_{2g} level ($E_x - E_z \equiv v$) and has nondiagonal matrix elements $\langle x|\hat{H}_{\rm trig}|v\rangle = \langle y|\hat{H}_{\rm trig}|w\rangle \equiv -v'$.

We have constructed Wannier functions via projection on the combinations of the $3d$-orbitals given by Eqs. (24). The values of the on-site Wannier matrix are given in the first four rows of Table VII. The LF parameters are then found by using

TABLE VII. Values (in meV) of the on-site Wannier matrix and the LF parameters of ZnO:Co to be used in $\hat{H}_{\mathrm{LF}}$. The LF parameters obtained by a Wannier fit are compared with two LF parameter sets obtained by fitting to optical spectra [59] or using a point charge model [60].

	$2\times2\times1$,	$2\times2\times2$,	Koidl[a]	Macfarlane[b]
$E_d - E_F$	−250.3	−278.6		
$E_x - E_d$	199.5	229.2	193.4	181.8
$E_z - E_d$	281.8	273.7	208.3	231.4
$E_v - E_d$	−340.4	−366.0	−297.6	−297.6
v'	−81.1	−52.7	−39.7	−43.4
v	−82.3	−44.5	−14.9	−49.6
Δ	567.4	610.0	495.9	495.9
B_4^0	−4.0	−4.65	−3.86	−3.74
B_4'	1.8	1.12	0.71	1.01
B_2'	7.0	4.98	4.64	3.48

[a]Reference [59].
[b]Reference [60].

the relations (see also [58]):

$$B_4^0 = \frac{1}{120}(E_v - E_x) \approx -4.6 \text{ meV},$$
$$B_4' = -\frac{1}{140}\left(E_x - E_z + \frac{3v'\sqrt{2}}{2}\right) \approx 1.1 \text{ meV},$$
$$B_2' = \frac{1}{21}\left(E_x - E_z - 2v'\sqrt{2}\right) \approx 5.0 \text{ meV}. \quad (25)$$

The Wannier functions of the fully relativistic non spin-polarized GGA functional lead to identical LF parameters and allow to calculate also the spin-orbit couplings. The corresponding on-site matrix shows medium deviations from spherical symmetry, in between the weak deviations for La_2NiO_4 and the strong ones for Li_2CuO_2. Since in the given case of a d^7 configuration all SOC matrix elements are important for the g factors and the multiplet spectrum, we take an average over the four different numerical values of SOC matrix elements to obtain $\zeta = 58.6$ meV, quite close to the value of 53.3 meV estimated by Koidl from a fit to the optical absorption spectra [59].

With these LF and SOC parameters, we calculated the multiplet spectrum, the zero field splitting (ZFS), the g factors, and the optical spectrum with the help of the ELISA code. The less critical Coulomb parameters $F^{(2)} = 7.65$ eV and $F^{(4)} = 5.46$ eV were taken as in Ref. [59]. These parameters lead to a reasonable agreement with the experimental multiplet spectrum, as visible in several absorption bands of ZnO:Co [59]. In Table VIII, we compare the average position of each band, i.e. the spectrum where SO coupling and trigonal distortion are neglected. The ELISA code reproduces also the fine structure very well which is demonstrated in Table IX for the $^4T_2$ absorption band lying in the infrared region.

The lowest $^4A_2$ multiplet of ZnO:Co corresponds to an effective spin 3/2 system with an easy plane anisotropy [58] visible in a zero field splitting (ZFS) between a lower and an upper doublet. In Table X, we compare ZFS and g-factors obtained from the ELISA code using Wannier parameters with experimental results, finding a good agreement in general.

TABLE VIII. Multiplet energies of Co^{2+} in ZnO as measured by optical absorption [59] in comparison to those calculated by the ELISA program with LF parameters from a Wannier fit. Tabulated are the main levels without fine structure.

Notation	Experiment [59] (eV)	This work (eV)
$^4A_2$	0.00	0.00
$^4T_2$	0.51	0.61
$^4T_1$	0.84	1.05
^2E	1.88	1.95
$^4T_1$	2.04	2.21

A more precise comparison of the theoretical multiplet spectrum with the optical absorption spectra demands also the calculation of the dipole matrix elements which is done here following the approach of Sugano and Tanabe [24] (9). In the case of ZnO:Co, the parity breaking perturbation is due to the lack of inversion symmetry in the tetrahedron and the trigonal distortion. That perturbation can be expressed in terms of spherical harmonics in the form

$$V_{\mathrm{odd}} = B_3\left(\sqrt{\frac{5}{2}}Y_3^0 + Y_3^{+3} + Y_3^{-3}\right). \quad (26)$$

As in the experiment [59], we distinguished two polarizations, the linear π polarization along the z axis and the circular polarizations σ_+ and σ_- within the x-y plane which are, however, identical without external magnetic field. We explain in Appendix D how the dipole matrix element (9) simplifies for these two polarizations and show in Fig. 7 the optical absorption with π and σ polarization for the $^4T_2$ band. In the upper panel, we choose LF parameters such that they represent the experimental spectra [59] in an optimal way ($\Delta = 465.7$ meV, $v = -14.9$ meV, and $v' = -39.7$ meV, being slightly improved with respect to the values given in Ref. [59]). The resulting curves coincide with the experimental spectra with respect to the peak positions and the relative heights but cannot reproduce the phonon side-band which is visible in the experimental spectra between 2.2 and 2.4 μm wavelength. In the lower panel of Fig. 7, we show the same $^4T_2$ band, but calculated with the Wannier parameter set. We find a good agreement with the upper panel and with experiment, besides

TABLE IX. Fine structure of the $^4T_2$ band in ZnO:Co; comparison between the ELISA multiplet calculation using parameters explained in the text and experimental date. The lowest level of the band has been set to zero in both cases.

Notation	This work (meV)	Experiment [59] (meV)
$E_{3/2}$	0.0	0.00
$E_{1/2}$	5.9	2.4
$E_{1/2}$	17.3	12.2
$E_{3/2}$	40.5	38.2
$E_{1/2}$	50.8	42.1
$E_{1/2}$	63.7	55.1

TABLE X. Comparison of g-factors and ZFS of Co^{2+} in ZnO.

	This work	Sati [57]	Koidl [59]
ZFS/cm^{-1}	5.98	5.52	5.4
g_z	2.22	2.236	
$g_x = g_y$	2.25	2.277	

a general shift of about 0.75 μm due to an overestimation of the cubic LF splitting Δ in the Wannier fit.

E. Actinide oxyde UO_2

To test the applicability of our approach to a $5f$-electron system, we have chosen UO_2, whose importance as a nuclear fuel makes it an object of intensive studies. It is an antiferromagnetic insulator. However, that is not correctly reproduced by standard spin-polarized DFT calculations without Hubbard U correction (LSDA or SGGA functionals) [63] who find metallic behavior. To obtain correct total energies for the study of point defects, diffusion, or thermodynamic properties it is important to combine the DFT+U functionals with the occupation matrix control [64] to avoid spurious local minima. In such a way, also the LF parameters of UO_2 had been calculated modifying the standard SGGA+U functional [14]. However, we will show now that the much more simple Wannier function method leads already to correct results.

The U^{4+} ion has $5f^2$ configuration and is surrounded by four oxygen ions forming an ideal tetrahedron. The ligand field has a cubic symmetry and is described by the effective Hamiltonian

$$\hat{H}_{\mathrm{LF,c}} = B_4\left(\hat{O}_4^0 + 5\hat{O}_4^4\right) + B_6\left(\hat{O}_6^0 - 21\hat{O}_6^4\right). \tag{27}$$

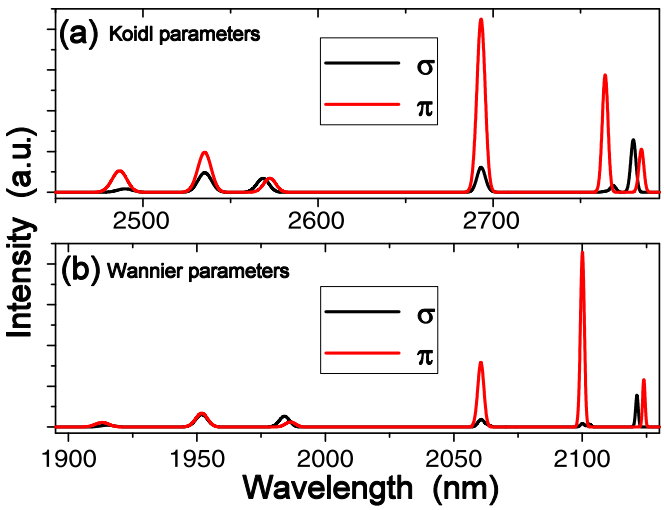

FIG. 7. Optical absorption spectra of the $^4T_2$ band in ZnO:Co with π and σ polarization as calculated from the ELISA code with parameters fitted to the experimental result [59] (a) or Wannier parameters (b). The width of the Gaussian broadening increases linearly from 0.1 to 1 meV going from lower to higher energies.

TABLE XI. The parameters and resulting energies (in meV) for UO_2.

	This work	LDA+U[a]	INS[b]	INS[c]
V_4	−146	−93	−123	−116.2
V_6	34	16	26.5	25.8
F^2	5339.3	5649	5339.3	
F^4	4562.9	3774	4562.9	
F^6	3607.2	2791	3607.2	
ζ	222.7	230	222.7	
Γ_5	0	0	0	0
Γ_3	165.1	125.7	150.1	150
Γ_4	169.7	156.3	166.7	158
Γ_1	175.5	174.0	174.8	170

[a]Reference [14].
[b]Reference [61].
[c]Reference [62].

The common notations for its two parameters are [61,65]

$$B_4 \equiv V_4\beta, \quad \beta = \frac{2}{11\cdot 45}, \tag{28}$$

$$B_6 \equiv V_6\gamma, \quad \gamma = -\frac{4}{11\cdot 13\cdot 27}. \tag{29}$$

To perform the Wannier fit we use the non-spin-polarized GGA band structure of UO_2 (not shown). There, the $5f$ bands are localized close to the Fermi energy and well separated from the rest of the spectrum. Using an energy window between −1.0 and 2.2 eV, we find the Wannier function on-site matrix given in Table XVI. The Wannier functions are found by projecting onto $5f$ real spherical harmonics, as defined in Ref. [22]. The on-site Wannier matrix can be easily diagonalized leading to the exact analytical eigenvalues and eigenfunctions given in Ref. [65]. The eigenenergies of the on-site Wannier matrix in the notation of Ref. [65] are (in meV) $E(\Gamma_2) = 1212.0 + \varepsilon_F$, $E(\Gamma_5) \equiv E(\Gamma_2) + V = 318.3 + \varepsilon_F$ and $E(\Gamma_4) \equiv E(\Gamma_2) + V' = 393.9 + \varepsilon_F$. From these energy differences, one can calculate the LF parameter values using the exact expressions of Ref. [65]:

$$B_4 = \frac{-V + 3V'}{2640}, \tag{30}$$

$$B_6 = \frac{9V - 5V'}{110\,880}. \tag{31}$$

The so obtained LF parameters are compared in Table XI with those obtained by the elaborated LSDA+U calculation with occupation matrix control [14], and with parameter sets due to fitting to inelastic neutron scattering experiments [61,62]. The Wannier LF parameter are then also used in the ELISA program to calculate the multiplet structure of the $5f^2$ configuration. For simplicity, we used the same SO and Coulomb parameter as in [61]. The lowest multiplet of the $5f^2$ configuration is $^3H_4$ which is split by the cubic ligand field into the levels given in Table XI. We find a very good agreement despite the numerical simplicity of our approach.

IV. DISCUSSION

The good agreement between our *ab initio* calculated LF parameters and experimentally well established values for the treated examples demonstrates that there are indeed only two main contributions to the LFs: the electrostatic potential in the crystal and hybridization to the neighboring ligands (see also Refs. [66,67]). One can also conclude that the electron-electron interaction has only a small influence. There is only one exception in the list of materials which we treated: it is ZnO:Co where the calculated cubic splitting Δ (or B_4^0) exceeds the experimental value considerably. The cubic splitting is mainly determined by the energy distance between d and p levels [58] which is probably not correctly calculated in GGA. It was shown by the authors of Ref. [12] that the relative position of the ligand levels with respect to the d or f bands is influenced by electron correlation effects for which they used this energy distance as a free parameter in their method to determine CF (or LF) parameters.

Due to the rather simple origin of the LF parameters it can also be expected that the filling of the d or f shell in otherwise similar compounds does not drastically change the LF parameters, reflecting their one-electron character. In that respect, it is instructive to compare the two treated tetragonal cases, La_2NiO_4 and $CaCuO_2$ which show a similar d-level ordering with one exception: the position of the d_{z^2} and d_{xy} orbitals are exchanged. That can be explained by the absence of the apex oxygen in the infinite layer compound $CaCuO_2$. Since it is just this apex oxygen which pushes the d_{z^2} level higher in energy such that it becomes most close to the $d_{x^2-y^2}$ orbital.

The results of our method depend in a sensitive way on the choice of the energy window for the Wannier fit. The dependence is less critical when the d or f band is well separated from the rest of the band structure as for UO_2, or when the overlap is small as for La_2NiO_4 or ZnO:Co. In these situations the energy window has just to encompass the relevant bands and increasing its width does not alter the LF parameters in a sensitive case as it is shown in Appendix C for ZnO:Co. The choice of the energy window is more critical when there is no clear separation as for $CaCuO_2$. In that case we fix the lower limit of the energy window such that it separates the antibonding d-like states from the bonding ones (see Appendix C), but there remains an error of the Wannier matrix elements H_{ii} which we estimate to be about 0.1 eV. In the case of a good separation the error is about ten times smaller.

We call our method *ab initio* but we do not understand that in the most strict sense. So, we propose to add a level broadening by hand to simplify the comparison with the experimental spectra. Also, we have shown that, occasionally, an adjustable exchange field improves the RIXS spectra for cuprates. This latter should be understood as arising from the antiferromagnetic nearest neighbor exchange couplings in the CuO_2 plane which are not explicitly included in our Hamiltonian, but nevertheless physically very well justified.

A possible improvement of our method is to relax the condition of spherical symmetry for SOC first, and after that also for the Coulomb interaction, two secondary effects of reducing the symmetry in the crystal. That introduces many new parameters, but the example of Li_2CuO_2 shows that they can be calculated from the Wannier fit. To perform an analogous procedure for the Coulomb interaction demands more work.

The method which we propose is close in spirit to Ref. [12] but applied here to less correlated $3d$ and $5f$ electrons in contrast to the $4f$ systems there. Treating the energy difference to the ligand levels as free parameter might sometimes improve the resulting LF parameters. However, in most cases which we considered, we found such a correction not necessary, except for ZnO:Co as mentioned above. Importantly, we do not only calculate the LF parameter, but also the multiplet spectra and many spectroscopical curves. That is similar to Ref. [17] where, however, the ligand orbitals are explicitely treated in the exact diagonalization procedure to calculate the multiplet spectra which breaks the relation to the traditionally known LF parameters.

V. CONCLUSION

We present a simple, general, and precise method of calculations of the multiplet spectrum and the relevant experimental spectra of local magnetic d and f centers in solids in an *ab initio* manner. The method combines the Wannier analysis of the nonmagnetic GGA band-structure with an exact diagonalization method of the local, atomic like, multiplet Hamiltonian containing Coulomb, spin orbit, and ligand field interactions. Despite its simplicity our method is remarkably precise. That gives us confidence to predict the multiplet structure of less well known systems. The precision we obtained is sufficient to classify the relevant spectroscopic terms.

ACKNOWLEDGMENTS

This work was supported by the National Academy of Sciences of Ukraine (Project No. III-4-19). We especially thank Manuel Richter and Liviu Hozoi for detailed discussions on the subject. We also thank Shi Lei, Ibrahim Mansouri, and Maen Salman for preliminary calculations at an early stage of the project, as well as Ulrike Nitzsche, Claude Arnold, and Andrey Likhtin for technical assistance, and the IFW Dresden (Germany) for the use of their computer facilities. We had valuable discussions with Valentina Bisogni, Yuri Ralchenko, Michael Kuzmin, and Michel Freyss on several subjects of the presented work, for which we are very grateful. O.J. was supported by the Leibniz Association through the Leibniz Competition.

TABLE XII. On-site Hamiltonian H_{ii} obtained by wannierization of the full-relativistic band-structure for the experimental structure of La_2NiO_4. All values are in meV.

	$\|xy,\uparrow\rangle$	$\|yz,\uparrow\rangle$	$\|3z^2-r^2,\uparrow\rangle$	$\|xz,\uparrow\rangle$	$\|x^2-y^2,\uparrow\rangle$	$\|xy,\downarrow\rangle$	$\|yz,\downarrow\rangle$	$\|3z^2-r^2,\downarrow\rangle$	$\|xz,\downarrow\rangle$	$\|x^2-y^2,\downarrow\rangle$
$\langle xy,\uparrow\|$	−1250.1	21.9	$-0.2i$	$-4.3i$	$69.7i$	0.0	$-26.0-26.0i$	0.0	$-25.7+25.7i$	$-5.4+5.4i$
$\langle yz,\uparrow\|$	21.9	−1193.7	$-6.0i$	$39.0i$	$-2.9i$	$26.0+26.0i$	0.0	$-45.5+45.5i$	$-2.4+2.4i$	$-25.3+25.3i$
$\langle 3z^2-r^2,\uparrow\|$	$0.2i$	$6.0i$	−130.6	3.0	6.1	0.0	$45.5-45.5i$	0.0	$45.9+45.9i$	0.0
$\langle xz,\uparrow\|$	$4.3i$	$-39.0i$	3.0	−1195.8	−0.5	$25.7-25.7i$	$2.4-2.4i$	$-45.9-45.9i$	0.0	$25.6+25.6i$
$\langle x^2-y^2,\uparrow\|$	$-69.7i$	2.9i	6.1	−0.5	333.4	$5.4-5.4i$	$25.3-25.3i$	0.0	$-25.6-25.6i$	0.0
$\langle xy,\downarrow\|$	0.0	$26.0-26.0i$	0.0	$25.7+25.7i$	$5.4+5.4i$	−1250.1	21.9	$0.2i$	$4.3i$	$-69.7i$
$\langle yz,\downarrow\|$	$-26.0+26.0i$	0.0	$45.5+45.5i$	$2.4+2.4i$	$25.3+25.3i$	21.9	−1193.7	$6.0i$	$-39.0i$	$2.9i$
$\langle 3z^2-r^2,\downarrow\|$	0.0	$-45.5-45.5i$	0.0	$-45.9+45.9i$	0.0	$-0.2i$	$-6.0i$	−130.6	3.0	6.1
$\langle xz,\downarrow\|$	$-25.7-25.7i$	$-2.4-2.4i$	$45.9-45.9i$	0.0	$-25.6+25.6i$	$-4.3i$	$39.0i$	3.0	−1195.8	−0.5
$\langle x^2-y^2,\downarrow\|$	$-5.4-5.4i$	$-25.3-25.3i$	0.0	$25.6-25.6i$	0.0	$69.7i$	$-2.9i$	6.1	−0.5	333.4

APPENDIX A: *AB INITIO* DETERMINATION OF SPIN-ORBIT COUPLING PARAMETERS

1. On-site Hamiltonians H_{ii} obtained by wannierization of full-relativistic band-structures of La_2NiO_4

The on-site Hamiltonians obtained by wannierization of the full-relativistic band-structures are given in Table XII for the experimental crystal structure and in Table XIII for the simplified crystal structure. The corresponding crystal structures are explained in the main text.

2. Spin-orbit interaction

The spin-orbit interaction Hamiltonian (6) may be rewritten as

$$\hat{H}_{\mathrm{SOC}} = \frac{\zeta}{2}\sum_i \left[2\hat{l}_i^z\hat{s}_i^z + \hat{l}_i^+\hat{s}_i^- + \hat{l}_i^-\hat{s}_i^+\right], \tag{A1}$$

where the summation goes over electrons. We will write its matrix in the basis of real spherical harmonics $|m,\sigma\rangle$, where $m = xy, yz, 3z^2-r^2, xz, x^2-y^2$, $\sigma = \pm 1/2$. The matrix element values

$$\langle m,\sigma|2\hat{l}^z\hat{s}^z + \hat{l}^+\hat{s}^- + \hat{l}^-\hat{s}^+|m',\sigma'\rangle = 2\sigma\delta_{\sigma,\sigma'}\langle m|\hat{l}^z|m'\rangle + \delta_{\sigma,-1/2}\delta_{\sigma',1/2}\langle m,|\hat{l}^+|m'\rangle + \delta_{\sigma,1/2}\delta_{\sigma',-1/2}\langle m|\hat{l}^-|m'\rangle \tag{A2}$$

are given in Table XIV. This matrix we compare with the nondiagonal part of the Hamiltonian matrix in the basis of Wannier functions obtained in the full-relativistic calculation for La_2NiO_4 (see previous section) and Li_2CuO_2 (Table XV). We may see that the full matrix of Li_2CuO_2 cannot be described by a single parameter ζ because the Wannier functions are not spherically symmetrical and has contributions from different sites. But to calculate the response of the system to the application of a magnetic field we need only the ground state Kramers doublet. This doublet contains the d_{xy} orbital with an admixture of other d_m orbitals coupled to it by the spin-orbit interaction. The exact diagonalization of the matrix gives the doublet wave functions

$$|\psi_0,\uparrow\rangle = 0.9993|xy,\uparrow\rangle - 0.0319i|x^2-y^2,\uparrow\rangle + 0.0134|yz,\downarrow\rangle + 0.0157i|xz,\downarrow\rangle, \tag{A3}$$

$$|\psi_0,\downarrow\rangle = 0.9993|xy,\downarrow\rangle + 0.0319i|x^2-y^2,\downarrow\rangle - 0.0134|yz,\uparrow\rangle + 0.0157i|xz,\uparrow\rangle. \tag{A4}$$

TABLE XIII. On-site Hamiltonian H_{ii} obtained by wannierization of the full-relativistic band-structure for the simplified structure of La_2NiO_4. All values are in meV.

	$\|xy,\uparrow\rangle$	$\|yz,\uparrow\rangle$	$\|3z^2-r^2,\uparrow\rangle$	$\|xz,\uparrow\rangle$	$\|x^2-y^2,\uparrow\rangle$	$\|xy,\downarrow\rangle$	$\|yz,\downarrow\rangle$	$\|3z^2-r^2,\downarrow\rangle$	$\|xz,\downarrow\rangle$	$\|x^2-y^2,\downarrow\rangle$
$\langle xy,\uparrow\|$	−1254.9	0.0	0.0	0.0	$69.2i$	0.0	36.8	0.0	$-36.8i$	0.0
$\langle yz,\uparrow\|$	0.0	−1200.4	0.0	$38.9i$	0.0	−36.8	0.0	$-64.3i$	0.0	$-35.3i$
$\langle 3z^2-r^2,\uparrow\|$	0.0	0.0	−131.2	0.0	0.0	0.0	$64.3i$	0.0	−64.3	0.0
$\langle xz,\uparrow\|$	0.0	$-38.9i$	0.0	−1200.4	0.0	$36.8i$	0.0	64.3	0.0	−35.3
$\langle x^2-y^2,\uparrow\|$	$-69.2i$	0.0	0.0	0.0	329.9	0.0	$35.3i$	0.0	35.3	0.0
$\langle xy,\downarrow\|$	0.0	−36.8	0.0	$-36.8i$	0.0	−1254.9	0.0	0.0	0.0	$-69.2i$
$\langle yz,\downarrow\|$	36.8	0.0	$-64.3i$	0.0	$-35.3i$	0.0	−1200.4	0.0	$-38.9i$	0.0
$\langle 3z^2-r^2,\downarrow\|$	0.0	$64.3i$	0.0	64.3	0.0	0.0	0.0	−131.2	0.0	0.0
$\langle xz,\downarrow\|$	$36.8i$	0.0	−64.3	0.0	35.3	0.0	$38.9i$	0.0	−1200.4	0.0
$\langle x^2-y^2,\downarrow\|$	0.0	$35.3i$	0.0	−35.3	0.0	$69.2i$	0.0	0.0	0.0	329.9

TABLE XIV. The matrix of SO interaction in the basis $|m, m_s\rangle$.

	$\|xy,\uparrow\rangle$	$\|yz,\uparrow\rangle$	$\|3z^2-r^2,\uparrow\rangle$	$\|xz,\uparrow\rangle$	$\|x^2-y^2,\uparrow\rangle$	$\|xy,\downarrow\rangle$	$\|yz,\downarrow\rangle$	$\|3z^2-r^2,\downarrow\rangle$	$\|xz,\downarrow\rangle$	$\|x^2-y^2,\downarrow\rangle$
$\langle xy,\uparrow\|$	0	0	0	0	$2i$	0	1	0	$-i$	0
$\langle yz,\uparrow\|$	0	0	0	i	0	-1	0	$-i\sqrt{3}$	0	$-i$
$\langle 3z^2-r^2,\uparrow\|$	0	0	0	0	0	0	$i\sqrt{3}$	0	$-\sqrt{3}$	0
$\langle xz,\uparrow\|$	0	$-i$	0	0	0	i	0	$\sqrt{3}$	0	-1
$\langle x^2-y^2,\uparrow\|$	$-2i$	0	0	0	0	0	i	0	1	0
$\langle xy,\downarrow\|$	0	-1	0	$-i$	0	0	0	0	0	$-2i$
$\langle yz,\downarrow\|$	1	0	$-i\sqrt{3}$	0	$-i$	0	0	0	$-i$	0
$\langle 3z^2-r^2,\downarrow\|$	0	$i\sqrt{3}$	0	$\sqrt{3}$	0	0	0	0	0	0
$\langle xz,\downarrow\|$	i	0	$-\sqrt{3}$	0	1	0	i	0	0	0
$\langle x^2-y^2,\downarrow\|$	0	i	0	-1	0	$2i$	0	0	0	0

The g factors entering in the effective spin-Hamiltonian (21) are then calculated as

$$g_\alpha = 2|\langle\psi_0,\uparrow|\hat{l}^\alpha + g_s\hat{s}^\alpha|\psi_0,\uparrow\rangle|. \tag{A5}$$

3. Rotation of the atomic spin-orbit coupling matrix

While the rotation of the full 10×10 matrix is cumbersome, it can be largely simplified if we restrict ourselves to the t_{2g} basis states. Here, the respective basis transformation reduces to the rotation of orbital angular momentum matrices $\mathbf{L}' \xrightarrow{\mathbf{R}} \mathbf{L}$ which can be done using conventional rotation matrices $\mathbf{R}$ (here, we rotate by $\frac{3}{4}\pi$ around the z axis):

$$H_{\mathrm{SOC}}^{t_{2g}} = \zeta\mathbf{L}'\cdot\mathbf{S} = \zeta\left(\mathbf{R}_{\frac{3\pi}{4}z}\mathbf{L}\mathbf{R}_{\frac{3\pi}{4}z}^{\mathsf{T}}\right)\cdot\mathbf{S}$$
$$= \frac{\zeta}{2}\left(\begin{array}{ccc|ccc} 0 & 0 & 0 & 0 & -\frac{\sqrt{2}}{2}-\frac{\sqrt{2}}{2}i & -\frac{\sqrt{2}}{2}+\frac{\sqrt{2}}{2}i \\ 0 & 0 & i & \frac{\sqrt{2}}{2}+\frac{\sqrt{2}}{2}i & 0 & 0 \\ 0 & -i & 0 & \frac{\sqrt{2}}{2}-\frac{\sqrt{2}}{2}i & 0 & 0 \\ \hline 0 & \frac{\sqrt{2}}{2}-\frac{\sqrt{2}}{2}i & \frac{\sqrt{2}}{2}+\frac{\sqrt{2}}{2}i & 0 & 0 & 0 \\ -\frac{\sqrt{2}}{2}+\frac{\sqrt{2}}{2}i & 0 & 0 & 0 & 0 & -i \\ -\frac{\sqrt{2}}{2}-\frac{\sqrt{2}}{2}i & 0 & 0 & 0 & i & 0 \end{array}\right). \tag{A6}$$

Here, $\mathbf{L}$ and $\mathbf{S}$ are orbital and spin angular momentum operators in the matrix form. The rotation matrix is given in the $(xy, yz, xz) = (z, x, y)$ basis and for the $\frac{3}{4}\pi$ rotation around z equals to

$$\mathbf{R}_{\frac{3\pi}{4}z} = \begin{pmatrix} 1 & 0 & 0 \\ 0 & -\frac{\sqrt{2}}{2} & \frac{\sqrt{2}}{2} \\ 0 & -\frac{\sqrt{2}}{2} & -\frac{\sqrt{2}}{2} \end{pmatrix}. \tag{A7}$$

TABLE XV. The matrix of the Hamiltonian (in meV) in the basis of Wannier functions obtained in the full-relativistic calculation for Li_2CuO_2.

	$\|xy,\uparrow\rangle$	$\|yz,\uparrow\rangle$	$\|3z^2-r^2,\uparrow\rangle$	$\|xz,\uparrow\rangle$	$\|x^2-y^2,\uparrow\rangle$	$\|xy,\downarrow\rangle$	$\|yz,\downarrow\rangle$	$\|3z^2-r^2,\downarrow\rangle$	$\|xz,\downarrow\rangle$	$\|x^2-y^2,\downarrow\rangle$
$\langle xy,\uparrow\|$	-171.31	0	0	0	$62.20i$	0	27.14	0	$-29.49i$	0
$\langle yz,\uparrow\|$	0	-2135.16	0	$39.44i$	0	-27.14	0	$-75.896i$	0	$-43.74i$
$\langle 3z^2-r^2,\uparrow\|$	0	0	-2456.79	0	0	0	$75.896i$	0	-75.83	0
$\langle xz,\uparrow\|$	0	$-39.43i$	0	-1989.89	0	$29.49i$	0	75.83	0	-44.24
$\langle x^2-y^2,\uparrow\|$	$-62.20i$	0	0	0	-2075.00	0	$43.74i$	0	44.24	0
$\langle xy,\downarrow\|$	0	-27.14	0	$-29.49i$	0	-171.31	0	0	0	$-62.20i$
$\langle yz,\downarrow\|$	27.14	0	$-75.896i$	0	$-43.74i$	0	-2135.15	0	$-39.44i$	0
$\langle 3z^2-r^2,\downarrow\|$	0	$75.896i$	0	75.83	0	0	0	-2456.79	0	0
$\langle xz,\downarrow\|$	$29.49i$	0	-75.83	0	44.24	0	$39.44i$	0	-1989.89	0
$\langle x^2-y^2,\downarrow\|$	0	$43.74i$	0	-44.24	0	$62.20i$	0	0	0	-2075.00

APPENDIX B: STEVENS OPERATORS

Traditionally, the one-particle ligand field Hamiltonian is expressed in terms of Stevens equivalent operators [65]. Here we give the formulas for operators that was used in this work. For d-electron systems, the ligand field is expressed via the operators of second

$$\hat{O}_2^0 = 3\hat{l}_z^2 - l(l+1), \quad \hat{O}_2^2 = \tfrac{1}{2}\left(\hat{l}_+^2 + \hat{l}_-^2\right), \tag{B1}$$

and fourth order

$$\hat{O}_4^2 = \tfrac{1}{4}\left\{\left[7\hat{l}_z^2 - l(l+1) - 5\right]\left(\hat{l}_+^2 + \hat{l}_-^2\right) + \left(\hat{l}_+^2 + \hat{l}_-^2\right)\left[7\hat{l}_z^2 - l(l+1) - 5\right]\right\}, \tag{B2}$$

$$\hat{O}_4^0 = 35\hat{l}_z^4 - 30l(l+1)\hat{l}_z^2 + 25\hat{l}_z^2 - 6l(l+1) + 3l^2(l+1)^2, \tag{B3}$$

$$\hat{O}_4^4 = \tfrac{1}{2}\left(\hat{l}_+^4 + \hat{l}_-^4\right), \tag{B4}$$

$$\hat{O}_4^3 = \tfrac{1}{4}\left\{\hat{l}_z\left(\hat{l}_+^3 + \hat{l}_-^3\right) + \left(\hat{l}_+^3 + \hat{l}_-^3\right)\hat{l}_z\right\}, \tag{B5}$$

where $\hat{l}_z$, $\hat{l}_+$, and $\hat{l}_-$ are angular momentum operators. For f-electron systems, the sixth-order operators appear

$$\begin{aligned}\hat{O}_6^0 = {} & 231\hat{l}_z^6 - 315l(l+1)\hat{l}_z^4 + 735\hat{l}_z^4 + 105l^2(l+1)^2\hat{l}_z^2 - 525l(l+1)\hat{l}_z^2 + 294\hat{l}_z^2 \\ & - 5l^3(l+1)^3 + 40l^2(l+1)^2 - 60l(l+1),\end{aligned} \tag{B6}$$

$$\hat{O}_6^4 = \tfrac{1}{4}\left\{\left(11\hat{l}_z^2 - l(l+1) - 38\right)\left(\hat{l}_+^4 + \hat{l}_-^4\right) + \left(\hat{l}_+^4 + \hat{l}_-^4\right)\left(11\hat{l}_z^2 - l(l+1) - 38\right)\right\}. \tag{B7}$$

APPENDIX C: CHOICE OF THE ENERGY WINDOW

Figure 8 illustrates the dependence of d-level splitting on the width of the Wannier functions energy window. The upper limit of the window is set to the top of the valence band for each compound. When we chose the window that includes only antibonding states, the splitting is much larger as compared with the case when the window includes all the states in the valence band. In the latter case, the splitting is due to the electrostatic potential only (the bare crystal field), whereas in the former case it also includes the hybridization contribution into the ligand field. The variation of on-site energies is very small for ZnO:Co when we vary the lower bound of the energy window between -0.75 and -2 eV since we are then in a gap of the density of states. That is not the case for the two cuprates where we choose the lower bound to be -3 eV separating in such a way antibonding and bonding states. However, there is no gap around -3 eV and we estimate an error of the on-site energies E_i of about 0.1 eV. The Gaussian width dE should be chosen as small as possible to reduce the error on E_i but a too small value of dE reduces the localisation of the Wannier orbitals. We have checked that the chosen values of dE are the optimal compromise between precision of E_i and localisation of Wannier orbitals.

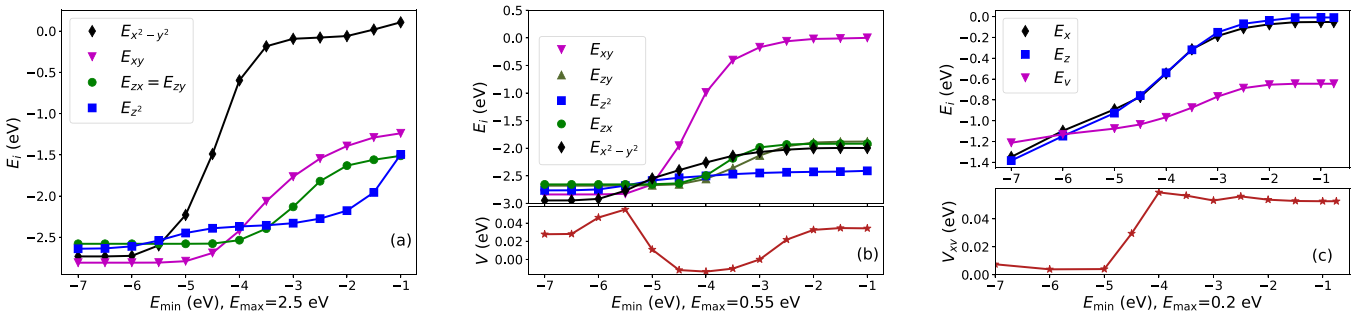

FIG. 8. The dependence of on-site energies of Wannier functions having d-function symmetry on the energy window for the compounds $CaCuO_2$ (a), Li_2CuO_2 (b), and ZnO : Co (c). The energy window is defined by a function being 1 between E_{min} and E_{max} and falling of as a Gaussian with a width $dE = 1$ eV outside this window for (a) and (b) and with a width $dE = 0.5$ eV for (c). The lower limit of the energy window which was really taken into account in our determination of LF parameters was -3 eV for (a) and (b) and -0.75 eV for (c).

TABLE XVI. The matrix of the on-site Hamiltonian (in meV) using the basis of real spherical harmonics for the Wannier expansion of UO_2.

	$\|5f,-3\rangle$	$\|5f,-2\rangle$	$\|5f,-1\rangle$	$\|5f,0\rangle$	$\|5f,+1\rangle$	$\|5f,+2\rangle$	$\|5f,+3\rangle$
$\langle 5f,-3\|$	365.58	0	36.62	0		0	0
$\langle 5f,-2\|$	0	1212.03	0	0	0	0	0
$\langle 5f,-1\|$	36.62	0	346.67	0	0	0	0
$\langle 5f,0\|$	0	0	0	393.94	0	0	0
$\langle 5f,+1\|$	0	0	0	0	346.67	0	−36.62
$\langle 5f,+2\|$	0	0	0	0	0	318.30	0
$\langle 5f,+3\|$	0	0	0	0	−36.62	0	365.58

APPENDIX D: DIPOLE MATRIX ELEMENTS OF OPTICAL TRANSITION

In this Appendix, we use the parity breaking perturbation (26) and follow Ref. [24] to express the dipole operator in the coordinate system

$$\vec{k}_+ = -\frac{1}{\sqrt{2}}(\vec{e}_x + i\vec{e}_y), \quad \vec{k}_- = +\frac{1}{\sqrt{2}}(\vec{e}_x - i\vec{e}_y), \quad \vec{k}_0 = \vec{e}_z, \tag{D1}$$

to be

$$\vec{P} = -P_+\vec{k}_- - P_-\vec{k}_+ + P_0\vec{k}_0, \tag{D2}$$

where the component $P_0 \propto Y_1^0$ and $P_\pm \propto Y_1^{\pm 1}$. Using the rules for coupling two angular momenta we can calculate the dipole matrix element for π polarization

$$W_0 \propto \left|\langle a|\left(\frac{9}{\sqrt{14}}Y_2^0 + \sqrt{\frac{40}{7}}Y_4^0 + Y_4^{+3} - Y_4^{-3}\right)|b\rangle\right|^2, \tag{D3}$$

and for σ polarization

$$W_\pm \propto \left|\langle a|\left(-\frac{3\sqrt{3}}{\sqrt{2}}Y_2^{\pm 1} + 5Y_4^{\pm 1} \pm \sqrt{28}Y_4^{\pm 4} \pm 3\sqrt{3}Y_2^{\mp 2} \mp Y_4^{\mp 2}\right)|b\rangle\right|^2. \tag{D4}$$

APPENDIX E: ON-SITE HAMILTONIAN H_{ii} FOR THE ACTINIDE OXYDE UO_2

The on-site Hamiltonian for uranium oxyde is given in Table XVI.

[1] H. A. Bethe, Splitting of terms in crystals, in *Selected Works of Hans A Bethe* (World Scientific, Singapore, 1997), p. 1.

[2] J. G. Bednorz and K. A. Mueller, Possible high T_c superconductivity in the Ba-La-Cu-O system, Z. Phys. B **64**, 189 (1986).

[3] N. Spaldin and R. Ramesh, Advances in magnetoelectric multiferroics, Nat. Mat. **18**, 203 (2019).

[4] S. Reschke, A. A. Tsirlin, N. Khan, L. Prodan, V. Tsurkan, I. Kézsmárki, and J. Deisenhofer, Structure, phonons, and orbital degrees of freedom in $Fe_2Mo_3O_8$, Phys. Rev. B **102**, 094307 (2020).

[5] C. Broholm, R. Cava, S. Kivelson, D. Nocera, M. Norman, and T. Senthil, Quantum spin liquids, Science **367**, eaay0668 (2020).

[6] N. Li, Q. Huang, X. Y. Yue, W. J. Chu, Q. Chen, E. S. Choi, X. Zhao, H. D. Zhou, and X. F. Sun, Possible itinerant excitations and quantum spin state transitions in the effective spin-1/2 triangular-lattice antiferromagnet $Na_2BaCo(PO_4)_2$, Nat. Commun. **11**, 4216 (2020).

[7] H. Liu, J. Chaloupka, and G. Khaliullin, Kitaev Spin Liquid in 3*d* Transition Metal Compounds, Phys. Rev. Lett. **125**, 047201 (2020).

[8] M. M. Sala, V. Bisogni, C. Aruta, G. Balestrino, H. Berger, N. B. Brookes, G. M. de Luca, D. D. Castro, M. Grioni, M. Guarise, P. G. Medaglia, F. M. Granozio, M. Minola, P. Perna, M. Radovic, M. Salluzzo, T. Schmitt, K. J. Zhou, L. Braicovich, and G. Ghiringhelli, Energy and symmetry of *dd* excitations in undoped layered cuprates measured by Cu L_3 resonant inelastic x-ray scattering, New J. Phys. **13**, 043026 (2011).

[9] G. Fabbris, D. Meyers, L. Xu, V. M. Katuruki, L. Hozoi, X. Liu, Z.-Y. Chen, J. Okamoto, T. Schmitt, A. Uldry, B. Delley, G. D. Gu, D. Prabhakaran, A. T. Boothroyd, J. van den Brink, D. J. Huang, and M. P. M. Dean, Doping Dependence of Collective Spin and Orbital Excitations in the Spin-1 Quantum Antiferromagnet $La_{2-x}Sr_xNiO_4$ observed by X-rays, Phys. Rev. Lett. **118**, 156402 (2017).

[10] L. Hozoi, L. Siurakshina, P. Fulde, and J. van den Brink, *Ab initio* determination of Cu 3*d* orbital energies in layered copper oxides, Sci. Rep. **1**, 65 (2011).

[11] L. Steinbeck, M. Richter, U. Nitzsche, and H. Eschrig, *Ab initio* calculation of electronic structure, crystal field, and intrinsic magnetic properties of Sm_2Fe_{17}, $Sm_2Fe_{17}N_3$, $Sm_2Fe_{17}C_3$, and Sm_2Co_{17}, Phys. Rev. B **53**, 7111 (1996).

[12] P. Novák, K. Knížek, and J. Kuneš, Crystal field parameters with Wannier functions: Application to rare-earth aluminates, Phys. Rev. B **87**, 205139 (2013).

[13] F. Zhou and D. Åberg, Crystal-field calculations for transition-metal ions by application of an opposing potential, Phys. Rev. B **93**, 085123 (2016).

[14] F. Zhou and V. Ozoliņš, Self-consistent density functional calculations of the crystal field levels in lanthanide and actinide dioxides, Phys. Rev. B **85**, 075124 (2012).

[15] J. P. Perdew, K. Burke, and M. Ernzerhof, Generalized Gradient Approximation Made Simple, Phys. Rev. Lett. **77**, 3865 (1996).

[16] L. Giovanelli, A. Savoyant, M. Abel, F. Maccherozzi, Y. Ksari, M. Koudia, R. Hayn, F. Choueikani, E. Otero, P. Ohresser, J.-M. Themlin, S. Dhesi, and S. Clair, XAS and XMCD measurements and theoretical analysis to detect the spin state in a Mn based metal-organic network, J. Phys. Chem. C **118**, 11738 (2014).

[17] M. W. Haverkort, M. Zwierzycki, and O. K. Andersen, Multiplet ligand-field theory using Wannier orbitals, Phys. Rev. B **85**, 165113 (2012).

[18] F. de Groot, Multiplet effects in x-ray spectroscopy, Coord. Chem. Rev. **249**, 31 (2005).

[19] E. Stavitski and F. de Groot, The CTM4XAS program for EELS and XAS spectral shape analysis for transition metal *L* edges, Micron **41**, 687 (2010).

[20] A. Kramida, Yu. Ralchenko, and J. R. and NIST ASD Team, NIST Atomic Spectra Database (ver. 5.8), [Online]. Available: https://physics.nist.gov/asd [2020, December 24]. National Institute of Standards and Technology, Gaithersburg, MD. (2020).

[21] (2018), FPLO-18 [improved version of the original FPLO code by K. Koepernik and H. Eschrig [22]]; http://www.FPLO.de.

[22] K. Koepernik and H. Eschrig, Full-potential nonorthogonal local-orbital minimum-basis band-structure scheme, Phys. Rev. B **59**, 1743 (1999).

[23] H. Eschrig and K. Koepernik, Tight-binding models for the iron-based superconductors, Phys. Rev. B **80**, 104503 (2009).

[24] S. Sugano, Y. Tanabe, and H. Kamimura, *Multiplets of Transition-Metal Ions in Crystals* (Academic Press, New York and London, 1970).

[25] N. Plakida, *High-Temperature Cuprate Superconductors: Experiment, Theory, and Applications* (Springer, Berlin, Heidelberg, 2010).

[26] L. Xu, *Ab initio* modeling of the electronic structure of d-metal systems and of resonant inelastic x-ray scattering responses, Ph.D. thesis, TU Dresden, Germany, 2019.

[27] J. Rodríguez-Carvajal, M. T. Fernández-Díaz, and J. L. Martínez, Neutron diffraction study on structural and magnetic properties of La_2NiO_4, J. Phys.: Condens. Matter **3**, 3215 (1991).

[28] M. I. Aroyo, D. Orobengoa, G. de la Flor, J. M. Perez-Mato, and H. Wondratschek, Brillouin-zone databases on the Bilbao Crystallographic Server, Acta Cryst. A **70**, 126 (2014).

[29] C. J. Ballhausen, *Introduction to Ligand-Field Theory*, Vol. 67 (Mac Graw-Hill Book Company, INC., New York, 1962), pp. 343–343.

[30] P. W. Anderson, The resonating valence bond state in La_2CuO_4 and superconductivity, Science **235**, 1196 (1987).

[31] M. Azuma, Z. Hiroi, M. Takano, Y. Bando, and Y. Takeda, Superconductivity at 110 K in the infinite-layer compound $(Sr_{1-x}Ca_x)_{1-y}CuO_2$, Nature (London) **356**, 775 (1992).

[32] A. S. Botana and M. R. Norman, Similarities and Differences Between $LaNiO_2$ and $CaCuO_2$ and Implications for Superconductivity, Phys. Rev. X **10**, 011024 (2020).

[33] J. Karp, A. S. Botana, M. R. Norman, H. Park, M. Zingl, and A. Millis, Many-Body Electronic Structure of $NdNiO_2$ and $CaCuO_2$, Phys. Rev. X **10**, 021061 (2020).

[34] L. J. P. Ament, G. Ghiringhelli, M. M. Sala, L. Braicovich, and J. van den Brink, Theoretical Demonstration of How the Dispersion of Magnetic Excitations In Cuprate Compounds can be Determined using Resonant Inelastic X-ray Scattering, Phys. Rev. Lett. **103**, 117003 (2009).

[35] H.-J. Mikeska and A. K. Kolezhuk, One-dimensional magnetism, in *Quantum Magnetism*, edited by U. Schollwöck, J. Richter, D. J. J. Farnell, and R. F. Bishop (Springer, Berlin, Heidelberg, 2004), pp. 1–83.

[36] S.-L. Drechsler, J. Richter, R. Kuzian, J. Málek, N. Tristan, B. Büchner, A. Moskvin, A. Gippius, A. Vasiliev, O. Volkova, A. Prokofiev, H. Rakoto, J.-M. Broto, W. Schnelle, M. Schmitt, A. Ormeci, C. Loison, and H. Rosner, Helimagnetism and weak ferromagnetism in edge-shared chain cuprates, J. Magn. Magn. Mater. **316**, 306 (2007), proceedings of the Joint European Magnetic Symposia.

[37] F. Sapiña, J. Rodríguez-Carvajal, M. J. Sanchis, R. Ibáñez, A. Beltrán, and D. Beltrán, Crystal and magnetic structure of Li_2CuO_2, Solid State Commun. **74**, 779 (1990).

[38] C. de Graaf, I. de P. R. Moreira, F. Illas, Ò. Iglesias, and A. Labarta, Magnetic structure of Li_2CuO_2 : From *ab initio* calculations to macroscopic simulations, Phys. Rev. B **66**, 014448 (2002).

[39] V. Yushankhai, L. Siurakshina, and R. Hayn, Ring exchange in transition metal oxides: A new manifestation in Li_2CuO_2? Physica B **312-313**, 726 (2002), the International Conference on Strongly Correlated Electron Systems.

[40] S. Kawamata, K. Okuda, and K. Kindo, ESR study on Li_2CuO_2 single crystal, J. Magn. Magn. Mater. **272-276**, 939 (2004), proceedings of the International Conference on Magnetism (ICM 2003).

[41] J. Málek, S.-L. Drechsler, U. Nitzsche, H. Rosner, and H. Eschrig, Temperature-dependent optical conductivity of undoped cuprates with weak exchange, Phys. Rev. B **78**, 060508(R) (2008).

[42] W. E. A. Lorenz, R. O. Kuzian, S.-L. Drechsler, W.-D. Stein, N. Wizent, G. Behr, J. Málek, U. Nitzsche, H. Rosner, A. Hiess, W. Schmidt, R. Klingeler, M. Loewenhaupt, and B. Büchner, Highly dispersive spin excitations in the chain cuprate Li_2CuO_2, EPL (Europhysics Letters) **88**, 37002 (2009).

[43] S. Nishimoto, S.-L. Drechsler, R. O. Kuzian, J. van den Brink, J. Richter, W. E. A. Lorenz, Y. Skourski, R. Klingeler, and B. Büchner, Saturation Field of Frustrated Chain Cuprates: Broad Regions of Predominant Interchain Coupling, Phys. Rev. Lett. **107**, 097201 (2011).

[44] C. Monney, V. Bisogni, K.-J. Zhou, R. Kraus, V. N. Strocov, G. Behr, J. Málek, R. Kuzian, S.-L. Drechsler, S. Johnston, A. Revcolevschi, B. Büchner, H. M. Rønnow, J. van den Brink, J. Geck, and T. Schmitt, Determining the Short-Range Spin Correlations in the Spin-Chain Li_2CuO_2 and $CuGeO_3$ Compounds Using Resonant Inelastic X-Ray Scattering, Phys. Rev. Lett. **110**, 087403 (2013).

[45] S. Nishimoto, S.-L. Drechsler, R. Kuzian, J. Richter, and J. van den Brink, Interplay of interchain interactions and exchange

anisotropy: Stability and fragility of multipolar states in spin-$\frac{1}{2}$ quasi-one-dimensional frustrated helimagnets, Phys. Rev. B **92**, 214415 (2015).

[46] S. Johnston, C. Money, V. Bisogni, K. Zhou, R. Kraus, G. Behr, V. N. Strocov, J. Málek, S.-L. Drechsler, J. Geck, T. Schmitt, and J. van den Brink, Electron-lattice interactions strongly renormalize the charge-transfer energy in the spin-chain cuprate Li_2CuO_2, Nat. Commun. **7**, 10653 (2016).

[47] C. Monney, V. Bisogni, K.-J. Zhou, R. Kraus, V. N. Strocov, G. Behr, S.-L. Drechsler, H. Rosner, S. Johnston, J. Geck, and T. Schmitt, Probing inter- and intrachain Zhang-Rice excitons in Li_2CuO_2 and determining their binding energy, Phys. Rev. B **94**, 165118 (2016).

[48] R. O. Kuzian, R. Klingeler, W. E. A. Lorenz, N. Wizent, S. Nishimoto, U. Nitzsche, H. Rosner, D. Milosavljevic, L. Hozoi, R. Yadav, J. Richter, A. Hauser, J. Geck, R. Hayn, V. Yushankhai, L. Siurakshina, C. Monney, T. Schmitt, J. Málek, G. Roth *et al.*, Comment on "Oxygen vacancy-induced magnetic moment in edge-sharing CuO_2 chains of Li_2CuO_2", New J. of Phys. **20**, 058001 (2018).

[49] W. E. A. Lorenz, On the spin-dynamics of the quasi-one-dimensional, frustrated quantum magnet Li_2CuO_2 studies by means of inelastic neutron scattering and thermodynamic methods, Ph.D. thesis, Technical University Dresden, 2011.

[50] N. A. Bogdanov, V. Bisogni, R. Kraus, C. Monney, K. Zhou, T. Schmitt, J. Geck, A. O. Mitrushchenkov, H. Stoll, J. van den Brink, and L. Hozoi, Orbital breathing effects in the computation of x-ray d-ion spectra in solids by *ab initio* wave-function-based methods, J. Phys.: Condens. Matter **29**, 035502 (2016).

[51] T. Dietl, H. Ohno, F. Matsukura, J. Cibert, and D. Ferrand, Zener model description of ferromagnetism in zinc-blende magnetic semiconductors, Science **287**, 1019 (2000).

[52] T. Dietl, A ten-year perspective on dilute magnetic semiconductors and oxides, Nat. Mater. **9**, 965 (2010).

[53] S. B. Ogale, Dilute doping, defects, and ferromagnetism in metal oxide systems, Adv. Mater. **22**, 3125 (2010).

[54] A. Simimol, A. A. Anappara, S. Greulich-Weber, P. Chowdhury, and H. C. Barshilia, Enhanced room temperature ferromagnetism in electrodeposited Co-doped ZnO nanostructured thin films by controlling the oxygen vacancy defects, J. Appl. Phys. **117**, 214310 (2015).

[55] T. Dietl, K. Sato, T. Fukushima, A. Bonanni, M. Jamet, A. Barski, S. Kuroda, M. Tanaka, P. N. Hai, and H. Katayama-Yoshida, Spinodal nanodecomposition in semiconductors doped with transition metals, Rev. Mod. Phys. **87**, 1311 (2015).

[56] R. O. Kuzian, J. Richter, M. D. Kuz'min, and R. Hayn, Lieb-Mattis ferrimagnetism in magnetic semiconductors, Phys. Rev. B **93**, 214433 (2016).

[57] P. Sati, R. Hayn, R. Kuzian, S. Régnier, S. Schäfer, A. Stepanov, C. Morhain, C. Deparis, M. Laügt, M. Goiran, and Z. Golacki, Magnetic Anisotropy of Co^{2+} as Signature of Intrinsic Ferromagnetism in ZnO : Co, Phys. Rev. Lett. **96**, 017203 (2006).

[58] R. O. Kuzian, A. M. Daré, P. Sati, and R. Hayn, Crystal-field theory of Co^{2+} in doped ZnO, Phys. Rev. B **74**, 155201 (2006).

[59] P. Koidl, Optical absorption of Co^{2+} in ZnO, Phys. Rev. B **15**, 2493 (1977).

[60] R. M. Macfarlane, Perturbation methods in the calculation of Zeeman interactions and magnetic dipole line strengths for d^3 trigonal-crystal spectra, Phys. Rev. B **1**, 989 (1970).

[61] G. Amoretti, A. Blaise, R. Caciuffo, J. M. Fournier, M. T. Hutchings, R. Osborn, and A. D. Taylor, $5f$-electron states in uranium dioxide investigated using high-resolution neutron spectroscopy, Phys. Rev. B **40**, 1856 (1989).

[62] H. Nakotte, R. Rajaram, S. Kern, R. J. McQueeney, G. H. Lander, and R. A. Robinson, Crystal fields in UO_2- revisited, J. Phys.: Conf. Ser. **251**, 012002 (2010).

[63] J. P. Crocombette, F. Jollet, L. T. Nga, and T. Petit, Plane-wave pseudopotential study of point defects in uranium dioxide, Phys. Rev. B **64**, 104107 (2001).

[64] B. Dorado, B. Amadon, M. Freyss, and M. Bertolus, DFT + U calculations of the ground state and metastable states of uranium dioxide, Phys. Rev. B **79**, 235125 (2009).

[65] A. Abragam and B. Bleaney, *Electron Paramagnetic Resonance of Transition Ions* (Dover Publications, New York, 1986).

[66] A. Savoyant, A. Stepanov, R. Kuzian, C. Deparis, C. Morhain, and K. Grasza, Single-ion anisotropy in Mn-doped diluted magnetic semiconductors, Phys. Rev. B **80**, 115203 (2009).

[67] A. Savoyant, A.-M. Daré, R. Hayn, R. Kuzian, and A. Stepanov, Hybridization and magnetic anisotropy of s-state ions in wurtzite DMS, physica status solidi (b) **247**, 1691 (2010).